

ABSTRACT

Title of Thesis: Experimental Study of
Segmented Constrained Layer Damping
in Rectangular and Sinusoidal Beams

Chinonso Oscar Ude
Master of Science, 2020

Thesis Directed by: Professor Norman M. Wereley
Department of Aerospace Engineering

In the aerospace engineering field, structures are constantly subjected to vibrations that are detrimental to the effectiveness and lifespan of the technology in use. In this work the performance of segmented constrained layer damping (SCLD) treatments for reducing vibration amplitudes is experimentally evaluated. In addition, two methods of manufacture and application are presented that employ 3D printed approaches. SCLD performance is evaluated by observing the bending response of cantilevered beams and the axial response of straight and sinuous springs. Measurements show that precise sample construction using a multi-jet modeling 3D printing approach and segment spacing based on a genetic optimization algorithm, leads to SCLD treatments that are effective for reducing vibration in cantilevered beams. Results also show that curved structures can also exploit SCLD treatments to enhance damping in axial springs, but that different algorithms for optimum segment size and spacing would be needed to create treatments that are tailored to the more complex spring structures.

Experimental Study of Segmented Constrained Layer Damping in
Rectangular and Sinusoidal Beams

by

Chinonso Oscar Ude

Thesis submitted to the Faculty of the Graduate School of the
University of Maryland, College Park in partial fulfillment
of the requirements for the degree of
Master of Science
2020

Advisory Committee:
Professor Norman Wereley, Chair/Advisor
Professor Alison Flatau
Professor Amr Baz
Professor Sung Lee

© Copyright by
Chinonso Oscar Ude
2020

Acknowledgments

I want to thank the University of Maryland for providing the environment and resources with which I've completed this degree. At UMD I've been blessed to encounter many people that I don't have the space here to properly address; from the lady who sold me muffins at the 24hr shop every week, to the friendliest cashier at the Stamp Union Shop, Mr. Wondamu.

I want to thank Ms. Rosemary Parker, director of the Center for Minorities in Science and Engineering, for encouraging me along this journey, and being a facilitator for many opportunities I received that have made me a prepared and more-detailed engineer. Thank you for empowering me to empower others!

I want to thank Dr. Jaret Riddick and Dr. Robert Haynes. Because of them I was able to find an internship opportunity at the Army Research Lab in Aberdeen, that ended up becoming the starting point for this entire thesis. You talked to me as a peer, and I can't tell you how much you impacted my confidence as a researcher.

I also appreciate the community I grew up in at the Composites Research Lab. Jon, Tom, Rebecca, Dr. Park, my dear friends Jacob and Jacek, and many more showed me how a graduate student is supposed to approach their work and carry them-self. I learned from you all often without you saying any words. I specially want to appreciate Jacob McCullum, Dale Martin, and Ehis Ebewe, with whom I struggled through many assignments.

Thank you to Dr. Alison Flatau and Dr. Amr Baz for serving on my committee! Thank you Dr. Flatau for helping me transition between the professional and research Master's degrees, you are one of the best "Emailing" professors I've ever met! Thank you Dr. Baz for telling me the hard truth when my homework was sloppy; the high standard you set is necessary in this world.

I want to thank my community of friends and family for encouraging me through this period, for helping me celebrate the successes, and learn from the failures. I want to acknowledge my parents, George and Assumpta Ude, as well as my siblings Onyedikachi and Amarachi Ude, for helping me forget I am a master's student many a time, but also helping me to remember.

I am grateful for the life and support of Dr. Norman Wereley. I'm not sure how this administrative stuff is supposed to work, but I've never seen anyone else receive the care and support that he has shown me since I met him in 2015. Maybe I'm just naive, but I marvel at the patience he's shown me as an instructor over the years, because I certainly have had my flaws and setbacks. Thank you Dr. Wereley for investing in me and for pushing me to be better, for saying when you didn't like something or when something didn't make sense, for making me go relearn myself about Mechanical Vibrations....and for the cookouts, I can't forget those.

Finally, I want to thank my God and savior Jesus Christ for saving me from my sins, and giving me a reason to live. Without him none of this would matter; the love of God has been my strength through this season.

Table of Contents

Preface	ii
Foreword	ii
Dedication	ii
Acknowledgements	ii
Table of Contents	iv
List of Tables	vi
List of Figures	vii
List of Abbreviations	ix
Chapter 1: Introduction	1
1.1 Motivation	1
1.2 Segmented Constrained Layer Damping	3
1.2.1 Optimization via Genetic Algorithms	6
1.3 Multi-jet Modeling	9
1.4 Axial Vibrations of Rectangular and Sinusoidal Springs	10
1.5 Scope of Thesis	14
Chapter 2: Damping Treatments of Cantilevered Beams	16
2.1 Introduction	16
2.2 MJM Beam Sample Fabrication	17
2.2.1 MJM Material Properties	17
2.3 Guiding Assumption	22
2.4 Test Setup	24
2.4.1 Approach to Data Analysis	26
2.5 MJM Test Results	28
2.6 Conclusions	30
2.7 Fused Deposition Modeling	31
2.8 FDM Material Properties	34
2.8.1 ABS Plastic	34
2.8.2 Sorbothane	35

2.9	Configuration Designs	36
2.9.1	SCLD Even Spaced Beam	38
2.9.2	Partially CLD Beam	38
2.9.3	Thicker 6.5 mm Beam	39
2.10	Test Results	40
2.11	Conclusions	42
Chapter 3: Damping Treatments for Sinusoidal Strut Springs		45
3.1	Beam Structure Overview	45
3.2	MJM Spring Sample Fabrication	46
3.3	Material Changes	48
3.3.1	RGD8530	48
3.3.2	FLX9795 (Transition Layer)	49
3.3.3	Rectangular Beam Spring	53
3.3.4	PCLD Rectangular Beam Spring	54
3.3.5	PCLD Sinusoidal Spring	55
3.4	Spring Test Setup	57
3.4.1	Steady State Response Test	60
3.4.2	Transient Response Test	61
3.4.3	Half Power Method	62
3.5	Test Results	62
3.5.1	MJM Temperature Effects	62
3.5.2	FDM + Hand-layup Spring Results	69
Chapter 4: Conclusions		77
4.1	Beam Experimentation (Phase 1)	77
4.2	Sinusoidal Spring Experimentation (Phase 2)	78
4.3	Future Work and Research Implications	79
Appendix A Material Data Sheets		82
A.1	Material Properties	82
A.1.1	VeroWhite	83
A.1.2	Agilus30	83
A.1.3	ABSplus	84
A.1.4	Sorbothane	84
A.1.5	RGD8530	84
A.1.6	FLX9795	85
Appendix B: Analytical Methods for extracting Damping Ratio		86
B.1	Log Decrement Damping Ratio	86
B.2	Half Power Method Damping Ratio	90
Bibliography		92

List of Tables

2.1	MJM Beam Materials	19
2.2	Percent Increase in Damping Ratio amongst MJM Beams	30
2.3	FDM Beam Materials	35
3.1	MJM Spring Materials	50
3.2	FDM Hand-layup Spring Materials	55
3.3	Percent Increase in Steady State Damping Ratio amongst MJM Springs	69
3.4	Percent Increase in Transient Damping Ratio amongst MJM Springs	69
A.1	Assumed Poisson Ratio's	82
A.2	VeroWhite	83
A.3	Agilus30	83
A.4	ABSplus	84
A.5	Sorbothane	84
A.6	RGD8530	84
A.7	FLX9795	85

List of Figures

1.1	Computer Aided Design of CLD Sample. TOP: Tough Constraining Layer, MID: Viscoelastic Shear Deformation Layer, BOT: Beam Base Layer	3
1.2	Visual representation of shear deformation in the form of shear angle λ	5
1.3	CAD Beam Configurations (Left to Right): Untreated, CLD, SCLD	5
1.4	Copies of Figures 3 and 6 from "Optimum design of segmented passive-constrained layer damping treatment through genetic algorithms" [1] Parameters from these two figures were used to select SCLD size and location, shown in the sketches to the right, used in the current study.	8
1.5	Visual Representation of Multi-jet Modeling Mechanics	9
1.6	Sinusoidal Spring: Effect of Axial Force on Shape	11
1.7	Sinusoidal Beam under 25 kg axial load	12
1.8	Sinusoidal Beam under 25 kg compressive load	13
2.1	MJM Beam with dimensions referenced in Fig. 1.4	19
2.2	Beam Configurations: Untreated (Top), CLD (Middle), SCLD (Bottom)	21
2.3	Layerwise Configuration	23
2.4	Beam Test Setup (Aerial and Side Views)	24
2.5	Beam Test Setup Simplified	26
2.6	Approach to Data Analysis	27
2.7	MJM Beam Damping Ratio Histograms (Transient Response)	28
2.8	Comparison between January, March and August Damping Ratios for MJM Beams RED indicates percent increase in damping from the Untreated case.	29
2.9	Fused Deposition Modeling Graphic	31
2.10	Example of fused deposition modeling and hand-layup process	33
2.11	SCLD Treatment Layup	36
2.12	Cantilever Beam Configurations (top view and cross section)	37
2.13	PCLD Beam Conception	38
2.14	Two Design Scenarios Compared	39
2.15	FDM + Hand-layup Damping Ratios (Transient Response)	41
2.16	Side View of a MJM SCLD Beam	43
2.17	Side View of an FDM SCLD Beam	43

2.18	Using Structural Design to Increase Damping	44
3.1	Shear Stress Distribution in Sinusoidal Beam	45
3.2	Sinusoidal Beam Wave Equation	47
3.3	Sinusoidal Beam Layerwise Configuration	47
3.4	Sinusoidal Beam Laminate Composition	48
3.5	MJM Sinusoidal Spring Configurations	50
3.6	FDM Sinusoidal Spring Components	52
3.7	Modifications Required for Load-bearing and Attachment to Shaker	53
3.8	CAD Models of Rectangular and Sinusoidal Beam Springs	54
3.9	FDM + Hand-layup Spring Configurations	56
3.10	Electrodynamic Shaker Test	57
3.11	Spring Test Setup Simplified	59
3.12	Approach to Data Analysis	60
3.13	Example of Steady State Response Test for 1st Mode of an MJM Sinusoidal Spring	61
3.14	Example of Transient Response Test for 1st Mode of an MJM Sinusoidal Spring	61
3.15	Untreated Spring Transfer Functions taken 5 Months Apart	64
3.16	CLD Spring Transfer Functions taken 5 Months Apart	65
3.17	SCLD Even Spaced Spring Transfer Functions taken 5 Months Apart	66
3.18	Comparison between March and August Damping Ratios (Steady State) for MJM Beams, RED indicates percent increase in damping from the Untreated case.	67
3.19	Comparison between March and August Damping Ratios (Transient) for MJM Beams, RED indicates percent increase in damping from the Untreated case.	68
3.20	Sinusoidal Spring Transmissibility Ratio as a result of Frequency Sweep (150-350 Hz)	70
3.21	Rectangular Spring Transmissibility Ratio as a result of Frequency Sweep (150-350 Hz)	71
3.22	Steady State transmissibility functions for Mode 1	72
3.23	Steady State Damping Ratios for Mode 1	72
3.24	Steady State transmissibility functions for Mode 2	73
3.25	Steady State Damping Ratios for Mode 2	73
3.26	Steady State transmissibility functions for Mode 3	74
3.27	Steady State Damping Ratios for Mode 3	74
3.28	Steady State Damping Ratios: A comparison between Rectangular and Sinusoidal Springs	75
B.1	Raw and Filtered Response Signals from Multi-jet Modeled Beams	87
B.2	Filtered Signals after Hilbert Transform is applied	88
B.3	Change of λ with respect to time	89
B.4	Half Power Method for Generating Damping Ratio from Transmissibility Ratio	91

List of Abbreviations

CLD	Constrained Layer Damping
CL	Constraining Layer
PCLD	Partially Constrained Layer Damping
SCLD	Segmented Constrained Layer Damping
FDM	Fused Deposition Modeling
VE	Viscoelastic
FEA	Finite Element Analysis
MJM	Multi-jet Modeling
SS	Sinusoidal
RB	Rectangular Beam
e	Displacement of Neutral Axis
r	Signal Peak-to-Peak Ratio
c	Log of r(Peak-to-Peak Ratio)
w	Beam Width
$F_{(a)}$	Applied Force

Chapter 1: Introduction

1.1 Motivation

In the aerospace, naval and automotive industries, Constrained Layer Damping (CLD) has come to play a pivotal role in suppressing vibrations. Evolving first from the use of viscoelastic (VE) damping tape, the addition of a constraining layer on the free surface of a VE tape made it so more vibration and wave propagation could be reduced with minimal and acceptable changes in thickness and mass. Applications that use CLD damping treatments include structures used in the naval and automotive industries primarily [2]. The premium here is the ability to convert mechanical energy into heat energy through deformation of the VE layer. CLD has been used to do this in both active and passive configurations on rotorcraft blades [3], submarines [2], and even construction drywall panels. Within the larger scope of CLD innovation, the addition of an active component through piezoelectrics has made the contribution of this technology even greater [4]. It was not until the 1960s that Ungar et al. [5] were able to formulate equations that quantified the ability of VE material to augment damping. Further progress since then has been actively pursued because of the great versatility, and low cost inherent in the method; particularly in the aerospace field, any benefit that does not come at the cost of weight is

welcomed. Covering the entire vibrating surface was proving to be inefficient [6], and at times difficult to accomplish on components with curved surfaces. In 1962, Parfitt showed that damping could be augmented by adding cuts in the VE layer, showing that weight could be reduced by cutting out sections of the damping layer. This, combined with research already done on the benefits of constrained VE layers [7], helped produce the Segmented Constrained Layer Damping method in the early 90s. This method has demonstrated advantages over the full treated CLD and partial CLD approaches [8] [3] and was further optimized for beams and plates in research by Plunkett, Lee [9], and Tian, Wu, Qin [10], and theoretically expanded upon with genetic algorithms by Al-Ajmi and Bourisli in 2008 [1]. Active piezoelectric damping in beams and like structures has been thoroughly pursued and validated in research like that of Baz and Ro [11]. Although Baz and Ro proved that the effectiveness of the viscoelastic sandwich beam can be substantially augmented with an active CL, the current research focuses on passive damping methods alone. It has been shown that CLD can be applied to complex (though arbitrary) structures for increased damping [12], and this work is a natural precursor to the experimentation with segmented treatments in this thesis. These segmented CLD treatments, referred to as SCLD, are even more versatile for structural damping because of the ability to separate treatments and account for sharp angles and small crevices in vibrating components. Theoretical studies on optimizing the design of SCLD treatments with genetic algorithms suggest performance gains that the current work will attempt to demonstrate with experiments. To that point, research involving applications of SCLD largely is done in one configuration: transverse displacement in cantilevered

beams and plate models. Identifying innovative ways in which to use SCLD to reduce axial vibrations is considered in the second half of this thesis with the goal of proving the usefulness of SCLD in non-standard applications. Fused Deposition Modeling (FDM) and Multi-jet Modeling (MJM) have been crucial parts of achieving the goals of this research, because of their ability to shape complex structures and damping treatments with high resolution at low cost. Parts that would otherwise have been glued together can be printed together in an assembly using MJM. The amount of time and cost saved in reproducing 3D printed samples is immense when you consider what is spent conventionally machining similar parts. The next few sections go further in depth into SCLD, FDM/MJM, and how these technologies were combined to test several different damping configurations.

1.2 Segmented Constrained Layer Damping

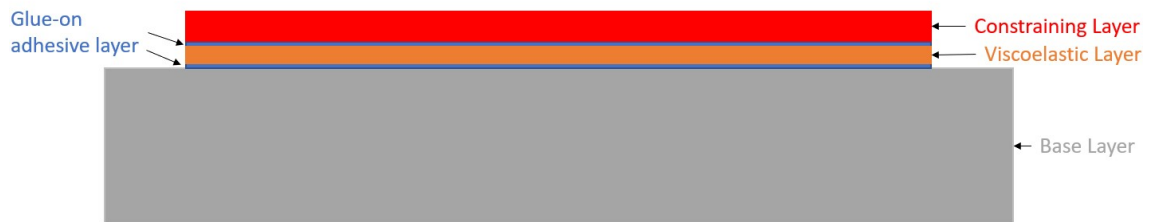


Figure 1.1: Computer Aided Design of CLD Sample. TOP: Tough Constraining Layer, MID: Viscoelastic Shear Deformation Layer, BOT: Beam Base Layer

Segmented Constrained Layer Damping (SCLD) is a method that has been proven to increase damping in vibrating structures under certain conditions; these require specific choice of layer to layer thickness ratios, VE material properties, the

number of segments, and the percentage of surface area covered. In CLD plates, the surface of the vibrating structure is treated with a VE material and then a stiff material [2], which increases damping of its oscillatory response to displacement. By adding a cut (s) through the VE and constraining layers, damping can be increased further under the right conditions; conditions being control of cut width, number of cuts, base layer to constraining layer height ratios, the range of shear motion induced, and relative elasticity between constrained and constraining layers. The SCLD treatment method involves applying segments or patches of CLD treatment selectively along a surface, be it a plate or beam. (See Fig. 1.1) The CLD treatment functions by turning shear strain into heat energy when the composite structure vibrates. The VE layer is where this process occurs as it is deformed under vibration between the constraining layer and the surface it is applied to.

When this technology was first being standardized in the 1960s, there were several terms used to quantify a composite's ability to dampen vibration. This parameter that characterizes the dynamics of the structure is commonly called a damping or loss factor [13], and the former will be used most in conjunction with "damping ratio" for the rest of this thesis. As previously mentioned, Parfitt showed that higher loss factors could be obtained by making cuts in the VE Layer. SCLD treatments take more advantage of the shear strain produced, by creating more shear angles along the length of the surface where the cuts are made. In contrast, a standard CLD treated beam would only have two shear sites dissipating energy at both ends of the beam CL (constraining layer). In Fig. 1.2 [14], the shear angle that occurs during deformation can be observed. The shear angle, or shear parameter,

is used to predict loss factor for simple beams or plates, and in turn damping ratio for CLD/SCLD treatments in this work.

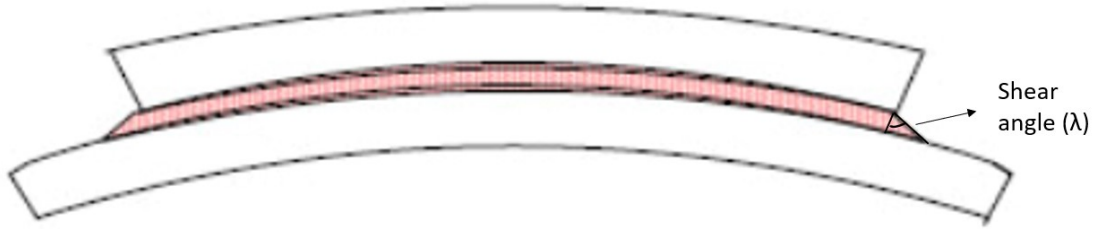


Figure 1.2: Visual representation of shear deformation in the form of shear angle λ

The work in this thesis considers a structure in untreated, CLD, and SCLD configurations (see Fig. 1.3). The SCLD treatments are effective alternatives to CLD under certain conditions. Layer Height, Shear Modulus of the VE Layer and Constraining Layer, SCLD Patch Length, and Cut Placement, are the primary factors that affect the damping ratio. In this research optimized values for cut location, layer height, and patch length are drawn from past works [1]. Finite Element Analysis (done with Siemens NX) is used to determine prime locations for placing cuts when it is deemed more fitting.

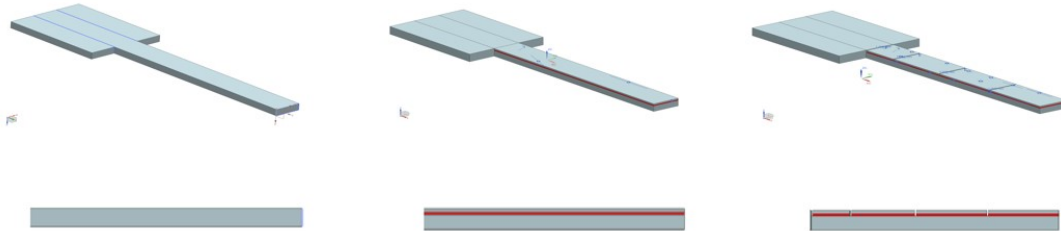


Figure 1.3: CAD Beam Configurations (Left to Right): Untreated, CLD, SCLD

1.2.1 Optimization via Genetic Algorithms

Genetic Algorithms have been used to optimize parameters in the field of biology [1], but in the research of Al-Ajmi and Bourisli, the number of cuts and evolution of cut locations along a damping treatment are used to maximize damping in a cantilevered rectangular beam by application of SCLD. It is important to note that before genetic algorithms were applied to CLD methods, it had been shown that a VE patch of specific length, location and thickness could be optimized to maximize damping of a sandwich beam [15], but the optimization presented here is not of the three layers present in a sandwich beam, but the two layers (VE and Constraining) added to an existing surface. A stochastic initial set of cuts is used to initialize an algorithm, that further iterates by assessing a loss factor generated by an FE model. The referenced FE model is verified for accuracy in the research of Kung et al. [16] [17]. The loss factor is the primary means of judging fitness for a given configuration output [18]. Fig. 1.4 displays two plots tracking the loss factor and the cut locations respectively for a given spread of constraining layer thicknesses. For a given h_2 thickness, there is computed an optimum treatment configuration for a range of h_1 thicknesses. The prior research showed that with a genetic algorithm, optimal values could be generated by controlling physical parameters like cut location and layer thickness to maximize loss factor. However it has remained to be seen whether such optimal cut locations and beam parameters can be effective experimentally. This thesis takes one configuration (referenced in the image) from previous research, seeking to examine how well the algorithm translates to experimental situations and

compares with other SCLD methods.

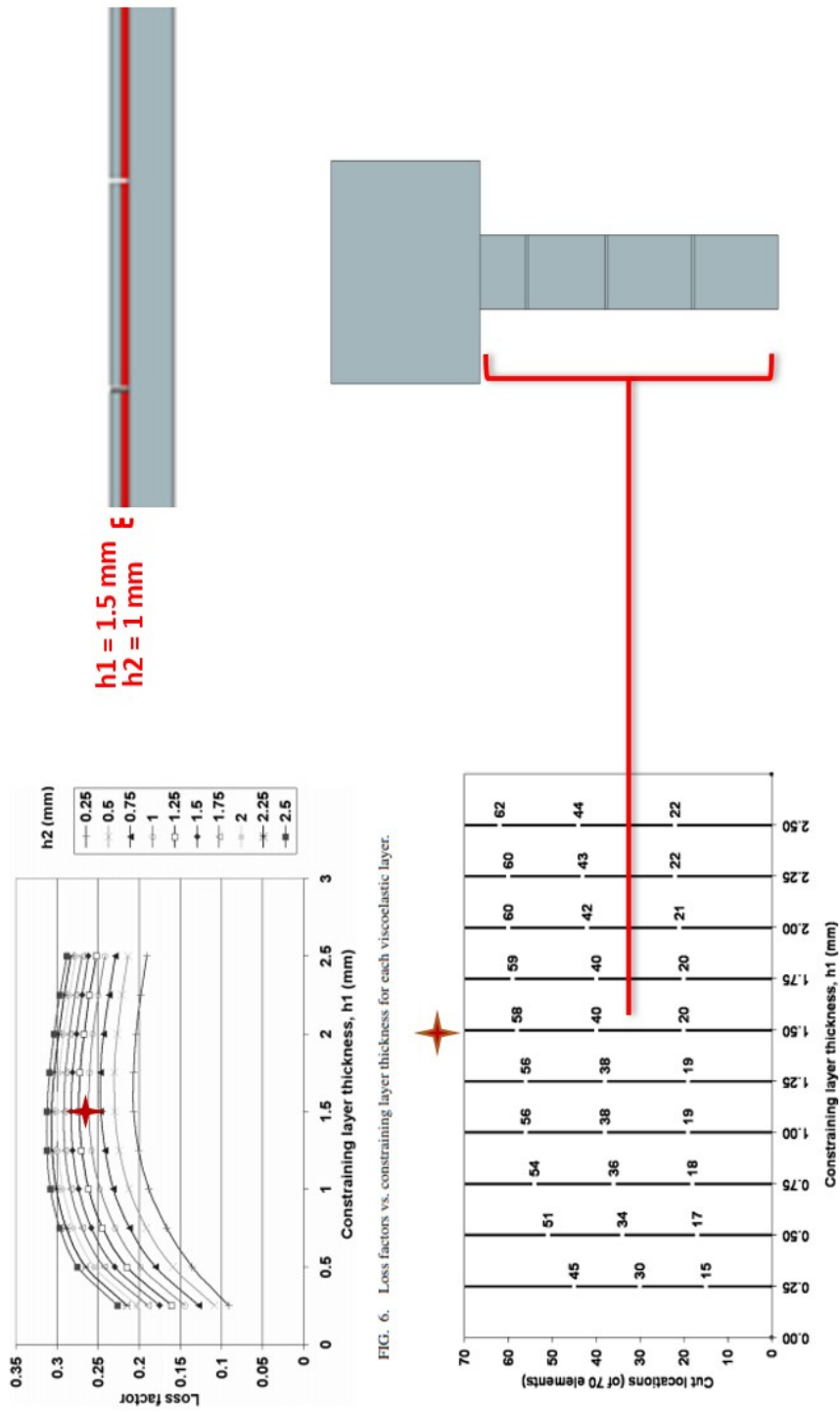


FIG. 6. Loss factors vs. constraining layer thickness for each viscoelastic layer.

FIG. 3. Optimal cut locations for various h_1 's for h_2 thickness of 1.00 mm.

Figure 1.4: Copies of Figures 3 and 6 from "Optimum design of segmented passive-constrained layer damping treatment through genetic algorithms" [1] Parameters from these two figures were used to select SCLD size and location, shown in the sketches to the right, used in the current study.

1.3 Multi-jet Modeling

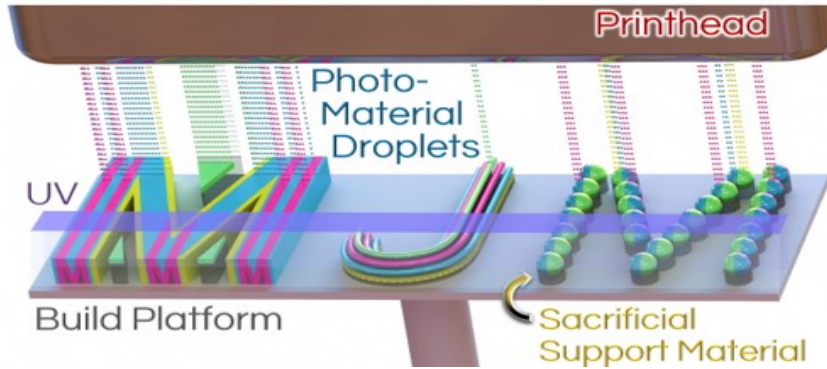


Figure 1.5: Visual Representation of Multi-jet Modeling Mechanics

Multi-jet Modeling (MJM) is a form of additive manufacturing that involves the jetting and ultraviolet curing of photo-reactive liquid. In Fig. 1.5 the primary components of the process are shown. This method of additive manufacturing is beneficial because of its very high resolution and material versatility. MJM allows for the simultaneous printing of different material properties and colors and it is this ability to print a part with both soft and hard components that makes MJM so suitable for generating damping treatments. This should shorten the manufacturing process and ensure that samples have structural integrity and geometric consistency upon testing. The printer used in this research is the Stratasys Connex Objet500, and it can reach resolutions of 16 microns, printing materials that can be as stiff as tough plastics or of comparable elasticity to rubber. The Objet500 employs a print bed volume of 490 x 390 x 200 mm and generates usable prints within a day or two depending on the complexity. In this research the MJM technology is compared with the FDM technology to determine how damping treatments can be more efficiently

and effectively manufactured using 3D printing.

1.4 Axial Vibrations of Rectangular and Sinusoidal Springs

In addition to reducing bending vibrations of slender structures, it can also be desirable to reduce the axial vibration of slender structures. Here, axial vibrations of two slender structures or "springs" are considered. One is a simple rectangular beam that is similar in shape to the cantilevered beam used in the transverse bending vibration studies. The other has the same cross section, but with a sinusoidal curvature along its length like the shape in Fig. 1.6. The sinusoidal structures examined in this research, take advantage of curvature along the length of the beam to induce greater shear in the VE layers, than in the simple rectangular spring. Because of this sinusoidal shape in elastic or VE materials more damping is generated with even very small axial displacements. The use of sinuous structures and VE materials in concert can add passive damping capabilities to axial springs that support dynamic loads. The undulating beam will be the main structural component of the sinusoidal springs (SS) studied in this thesis, drawing inspiration from studies by Dr. Robert Haynes [19].

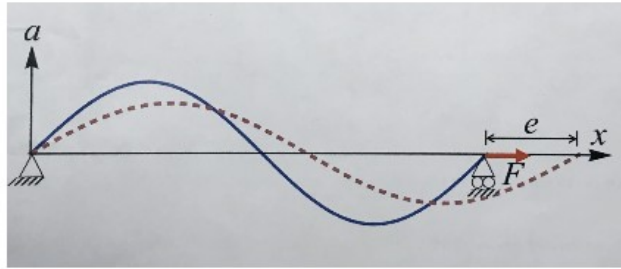


Figure 1.6: Sinusoidal Spring: Effect of Axial Force on Shape

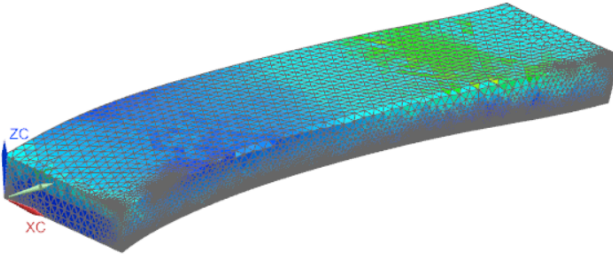
As the neutral axis is displaced by amount e , as shown in Fig. 1.6 the sinusoidal spring curvature changes dramatically. Though for stiff materials this change is minute, the shear stress produced still is useful and will be much greater than the change in curvature produced when compressing a straight rectangular spring by same displacement amount e . This produces more shear deformation in a VE layer attached to the beam's surface, and in turn, more damping.

In addition, an axial sinusoidal spring when loaded, is subjected to non-uniform shear forces along its length that suggest that combination with SCLD treatments may be more effective than CLD treatments. Fig. 1.8 shows a beam that is loaded in compression with the left hand side fixed. Under a load of 25 kg, regions of large shear stress develop along the peaks of the beams curves. These same areas are highly stressed in shear when the beam is axially loaded. Placing CLD and SCLD patches in these areas is theorized to take advantage of the shear motion induced by loading, to dampen vibration. For this research, placement of the damping treatments will consider these areas of high shear stress. Both methods will be used in testing samples, as is deemed appropriate.

plain_n1 : Solution 1 Result
Subcase - Static Loads 1, Static Step 1
Stress - Element-Nodal, Unaveraged, Max Shear
Min : 0.26, Max : 29.05, Units = MPa
Deformation : Displacement - Nodal Magnitude
Animation Frame 7 of 8



[MPa]



plain_n1 : Solution 1 Result
Subcase - Static Loads 1, Static Step 1
Stress - Element-Nodal, Unaveraged, Max Shear
Min : 0.26, Max : 29.05, Units = MPa
Deformation : Displacement - Nodal Magnitude
Animation Frame 8 of 8



[MPa]

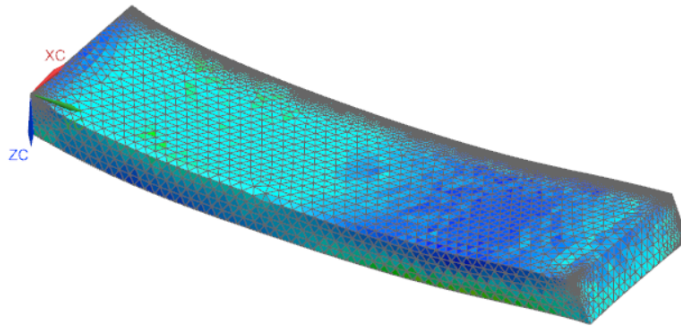
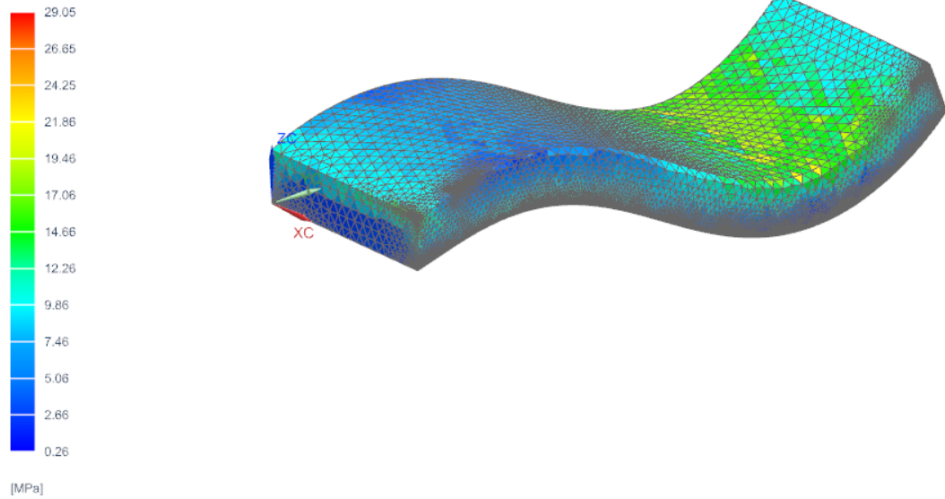


Figure 1.7: Sinusoidal Beam under 25 kg axial load

plain_n1 : Solution 1 Result
Subcase - Static Loads 1, Static Step 1
Stress - Element-Nodal, Unaveraged, Max Shear
Min : 0.26, Max : 29.05, Units = MPa
Deformation : Displacement - Nodal Magnitude
Animation Frame 8 of 8



plain_n1 : Solution 1 Result
Subcase - Static Loads 1, Static Step 1
Stress - Element-Nodal, Unaveraged, Max Shear
Min : 0.26, Max : 29.05, Units = MPa
Deformation : Displacement - Nodal Magnitude
Animation Frame 8 of 8

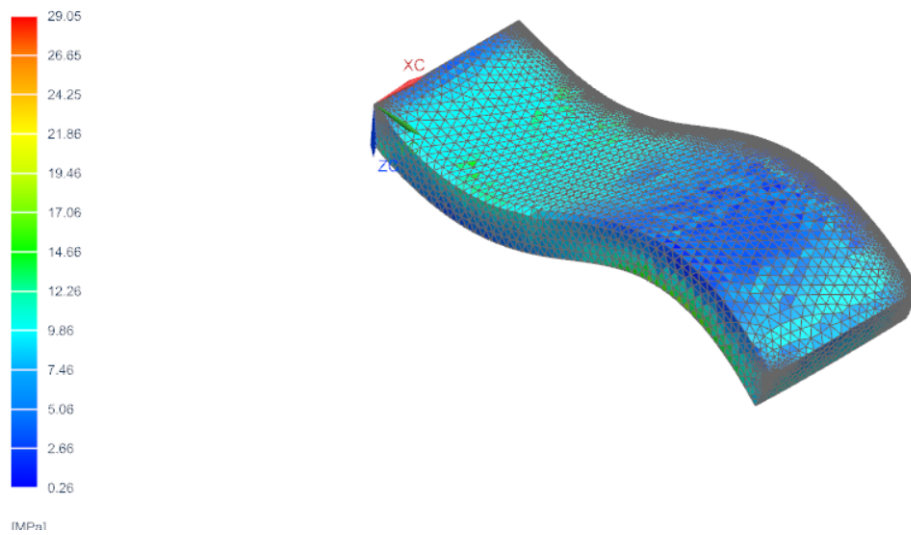


Figure 1.8: Sinusoidal Beam under 25 kg compressive load

1.5 Scope of Thesis

This thesis experimentally studies the effectiveness of optimized Segmented Constrained Layer Damping (SCLD) treatments on beams and sinusoidal structures. Two methods of building these samples are examined and compared as well. The evolution of application from beams to sinusoidal structures is studied, and results, though lacking consistency, show signs of increased damping. This thesis is meant to compare SCLD methods, while comparing approaches to 3D printing in the manufacturing process. This will bring concrete evidence to the discussion of how effective SCLD methods can be in beams and sinusoidal springs, as well as to the possibilities available with 3D printing and the CLD technology.

With that considered, the thesis is divided into two main phases.

Chapter 2 (Phase 1) will focus on damping treatments of cantilevered beams. The various CLD and SCLD treatments that are used will be carefully explained, and the methods of fabrication will be described as well. Relevant factors like material properties, layer thicknesses, and lengthwise cut locations will be explained in regards to how they impacted the designs. Analytical methods for extracting damping ratio like the Log Decrement and Hilbert Transform, will be introduced. Methods of 3D printing the beam laminates will be experimentally validated, with positives and negatives from each approach clearly laid out. Finally, information that proves relevant to the application to sinuous springs will be highlighted.

In Chapter 3 (Phase 2), the focus shifts to the application of (mostly) the same damping treatments to rectangular and sinusoidal axial springs. The axial spring

structures are introduced and explained, and exegesis of the various configurations deployed is given. Several material changes that are distinct from the Chapter 2 experiments are explained as well. The Half Power Method is explained as a tool for extracting damping ratio from steady state response data, and data from a range of modes is taken. The damping ratios from the sinusoidal springs are compared with data for the rectangular axial springs with respect to both the structural impact and treatment impact. Conclusions, along with potential for future work, drawn from this are elaborated upon in Chapter 4.

Chapter 2: Damping Treatments of Cantilevered Beams

2.1 Introduction

In the work of Kress [8], and Bourisli, we find conclusions based on Finite Element Analysis that support the benefits of different variations to the constrained layer damping method when used on cantilever beams. Kress showed that evenly spaced cuts added damping and were in most cases as effective as cuts placed via optimization (with respect to max bending moment). Bourisli showed that a genetic algorithm based on the optimization of modal loss factor can be of use in determining cut placement. This thesis takes these optimization methods to task in a specific way. As stated earlier, many factors affect the effectiveness of a damping treatment, be it complete or segmented. Cut width, layer to layer thickness ratio, beam material properties, viscoelastic material properties, constraining layer material properties, number of cuts, cut spacing, and the specific application of the damped device all will affect the performance of the treatment method. This chapter focuses on specific properties and parameters, comparing predicted FEA optimization-based designs with both standard and theoretical designs. Using the cantilever beam model that the optimized configurations are based on, comparison between SCLD application methods will be made.

If it can be experimentally proven that FEA based algorithms and optimization methods are viable, then it is easier for such methods to find mainstream applications. Testing such methods also helps with refinement and discovery of failure cases that a computation might not foresee.

Testing the damping treatment methods on cantilever beams is performed so that general trends can be observed that influence how we look at the vibratory response of structures with CLD and SCLD treatments. By creating a diverse sample size (see Fig. 2.12) in regards to which methods are compared, opportunity is created to assess the effectiveness of 3D printing in supporting the manufacturing process.

This chapter goes into detail concerning which optimization methods are being applied, what materials are being used, the manufacturing process, and the performance measures for each beam. Significant reasoning is provided to support these choices; challenges and sources of error in the design and experimentation are discussed as well. Finally, ways that successful treatments can be maximized in the field are explored.

2.2 MJM Beam Sample Fabrication

2.2.1 MJM Material Properties

A constrained layer damping treatment is generally made of three components:

- Base Beam Layer

- Viscoelastic (VE) Layer
- Rigid Constraining Layer

In the following sub-sections the materials used to represent these essential components are described and supported as to which needs they meet and why.

2.2.1.1 Agilus30

Agilus30 is a multi-jet photopolymer that resembles rubber in tear resistance and flexibility. Its ability to simulate rubber properties make it ideal for design validation and prototyping involving viscoelastic materials [20]. Agilus30 is used as the VE layer in the first set of MJM beams, and with a shear modulus of around 0.4 MPa, in contrast with VeroWhite, which has a shear modulus of around 925 MPa, provides a good context for testing SCLD.

2.2.1.2 VeroWhite

VeroWhite is a subset of the Vero material class used in the Connex Objet500. It was chosen because it is the stiffest (shear modulus of 925 MPa) [21] material the printer deploys, and therefore would produce the highest shear strains in the Agilus30 VE layer, and more damping as a result. It makes up both the Base Beam and Stiff Constraining Layers.

Materials	Young's Modulus (MPa)	Shear Modulus (MPa)
VEROWHITE	2500	925.9
AGILUS30	1.265	0.427

Table 2.1: MJM Beam Materials

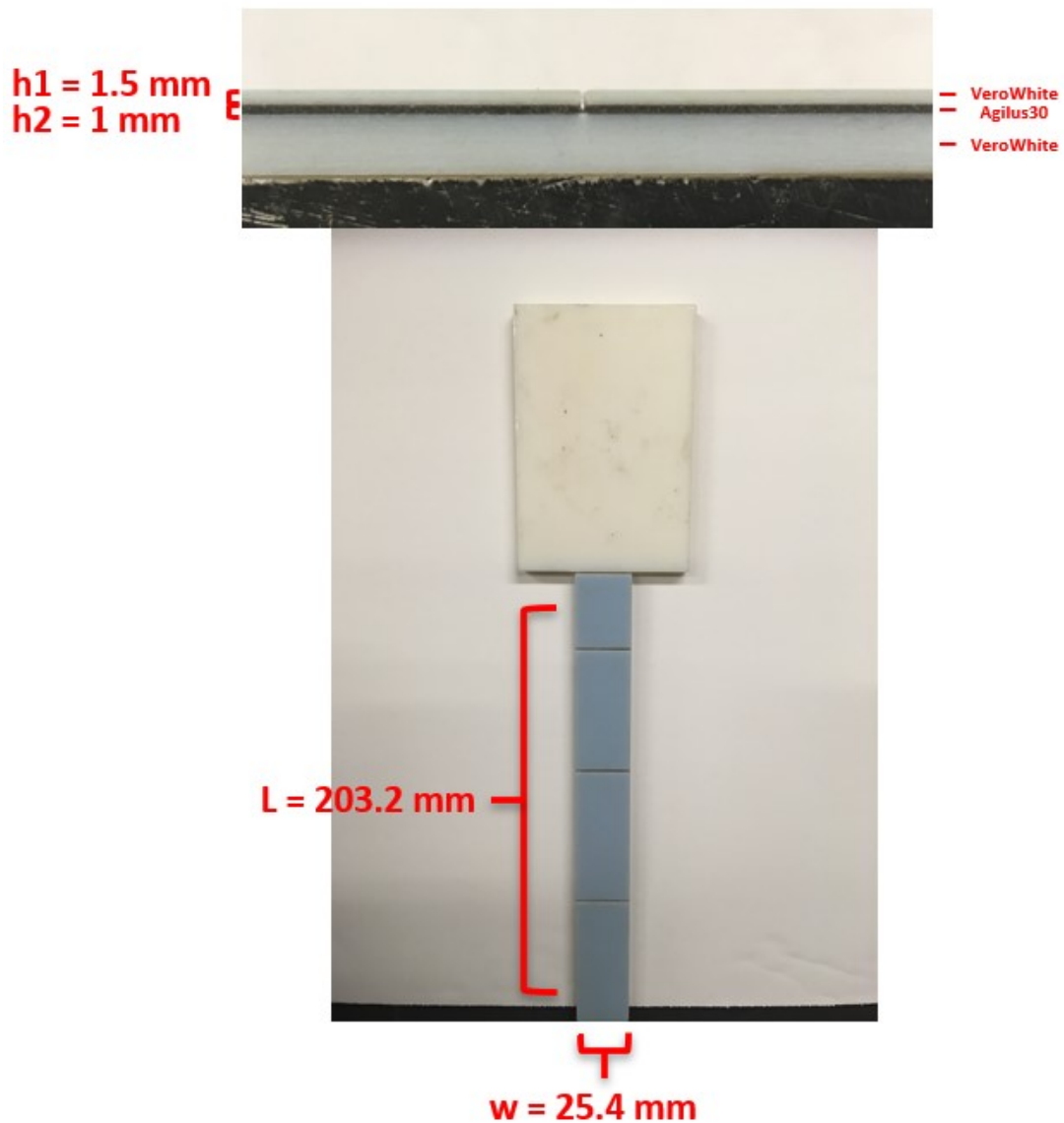


Figure 2.1: MJM Beam with dimensions referenced in Fig. 1.4

The MJM Beam samples were printed each as one piece composed of two ma-

materials, Agilus30 and VeroWhite. These proprietary materials combine to allow for high shear stresses in the beam between the two materials. The dimensions derived from previous research are $h_1 = 1.5mm$, and $h_2 = 1.0mm$, with L and w being chosen arbitrarily for the purpose of creating slender beams. The number of cuts was taken from the optimized configuration based on the work in [1], corresponding with the highest loss factor for the VE layer thickness of 1.0 mm. The cut width was chosen to be wide enough so that the 3D printer could craft the features cleanly and without loose strands of interconnected material. Though the Connex Objet500 is said to have a resolution that is as high as 16 microns [22], the width of 1.0 mm was meant to be cautious due to the many ways such a distance can be compromised even in a highly capable machine. At times when a distance is very small and support material is used, it (the support material or build material itself) can get clogged in crevices and detailed features of a part where it shouldn't be. Once again, the cut width of 1.0 mm was chosen to avoid this issue.

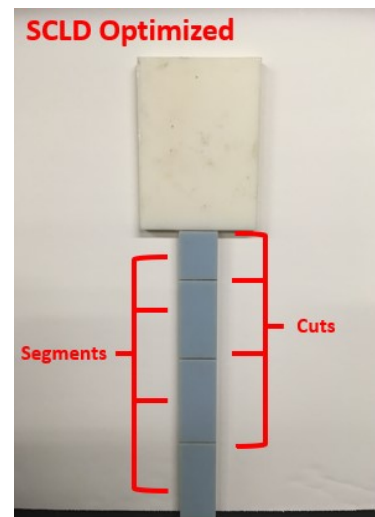


Figure 2.2: Beam Configurations: Untreated (Top), CLD (Middle), SCLD (Bottom)

The first round of testing involved three configurations (Fig. 2.2). The untreated beam is purely VeroWhite plastic, the CLD beam is completely covered by a VE layer, and another plastic layer on top, and the SCLD Optimized beam has cuts taken from the configuration already pictured in Fig. 2.1.

2.3 Guiding Assumption

A general assumption made in the manufacturing of these sandwich beams is that

$$E_1 H_1^3 / E_3 H_3^3 < 1.0$$

This assumption is one of several used by Kerwin [7] when he derived a theory that predicted the loss factor for constrained viscoelastic layers. For cantilevered beams, Kerwin's research has become foundational. It must be noted that the layer label conventions are opposite of those used by Al-Ajmi and Bourisli, with h_1 (previously the top constraining layer) as the base layer, and h_3 as the topmost constraining layer. Fig. 2.3 displays the labeling convention used for this assumption.

For VeroWhite,

$$E_1 = E_3 = 2.5GPa,$$

and a height of 4.0 mm was selected for h_3 in order to keep within the range of the assumption. After applying this and the respective heights we find that.

$$E_1 H_1^3 / E_3 H_3^3 = 0.0527 < 1.0$$

As a result, a base beam layer of 4.0 mm is used throughout the research except where otherwise noted. When keeping the material for beam and constraining layers the same, only the relative heights need be adjusted in order to assure that layers do not separate due to a disparity in shear strain in the VE laminate.

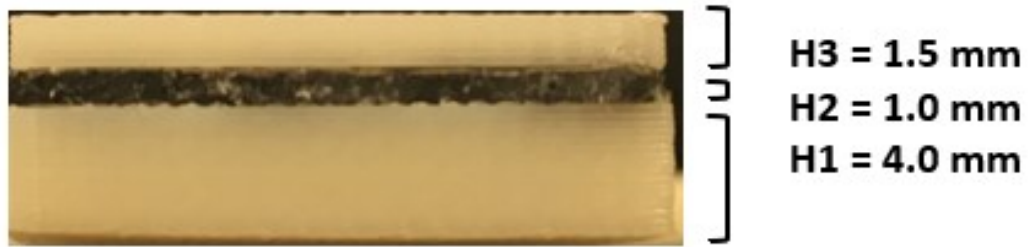


Figure 2.3: Layerwise Configuration

2.4 Test Setup

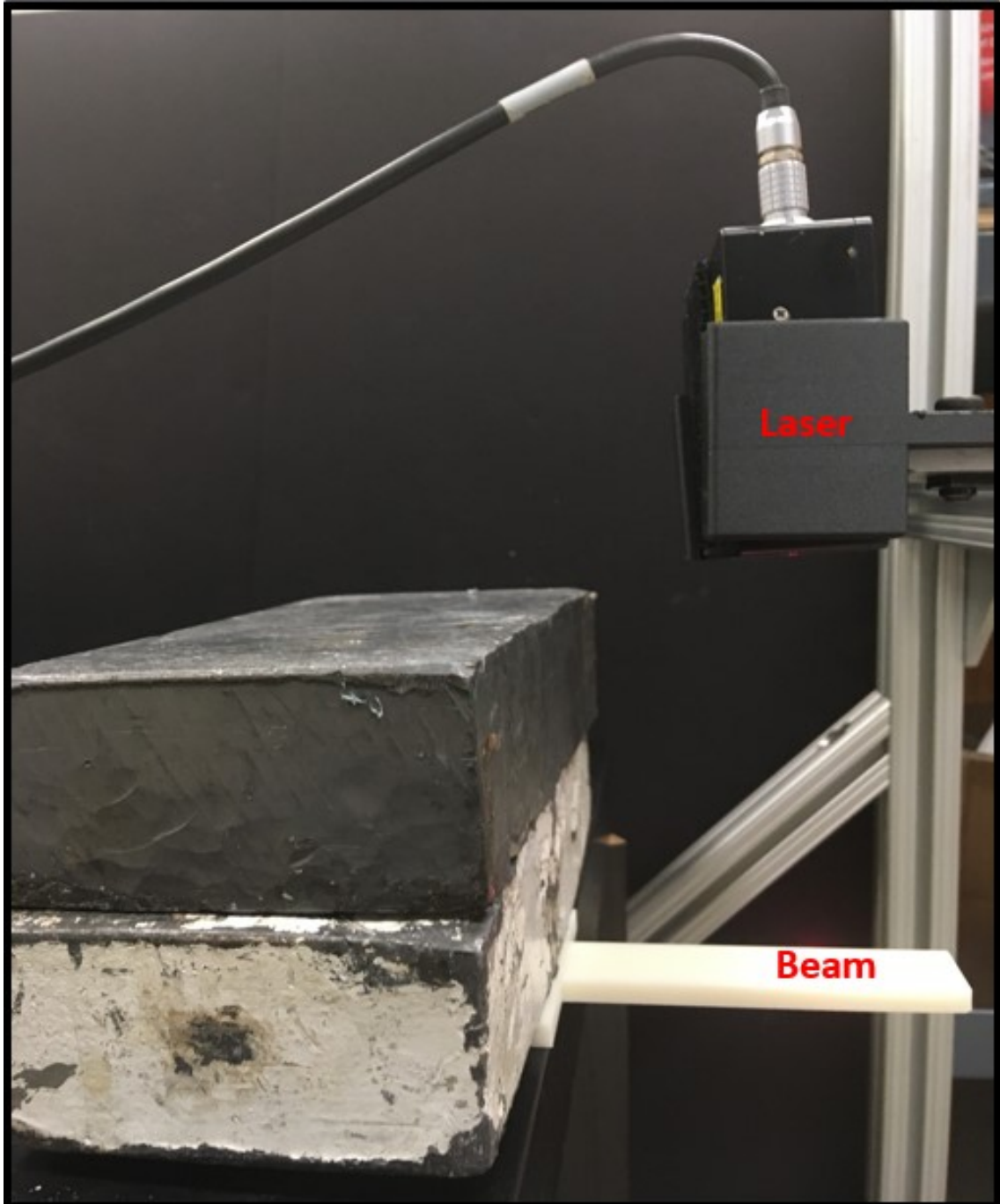


Figure 2.4: Beam Test Setup (Aerial and Side Views)

In Fig. 2.4 there is a side view of the test setup used to capture the transient responses of treated cantilever beams. It is included to better show how a clamped root condition was approached for the beam. The mass of the two bricks was about 20 kg each and they were used to keep the beam root stationary at the time of impulse. The MTI Microtrak Analog laser is held up using a fixture made with 80/20 aluminum. Fig. 2.5 shows a schematic of the setup, showing how the static deflection and resulting oscillations are collected as a voltage signal with the data acquisition device. The image shows the power supply for the analog laser, the laser itself, and the National Instruments Data Acquisition equipment. Each initial tip deflection was done by hand and estimated to be between 7 to 8 mm in magnitude. Tests were repeated to make sure that static offsets were kept consistent for each beam. The laser recorded displacement by tracking changes in voltage and the signal is recorded and processed using National Instruments Signal Express software at a sample rate of 25000 Hz and over a period of 5-10 seconds.

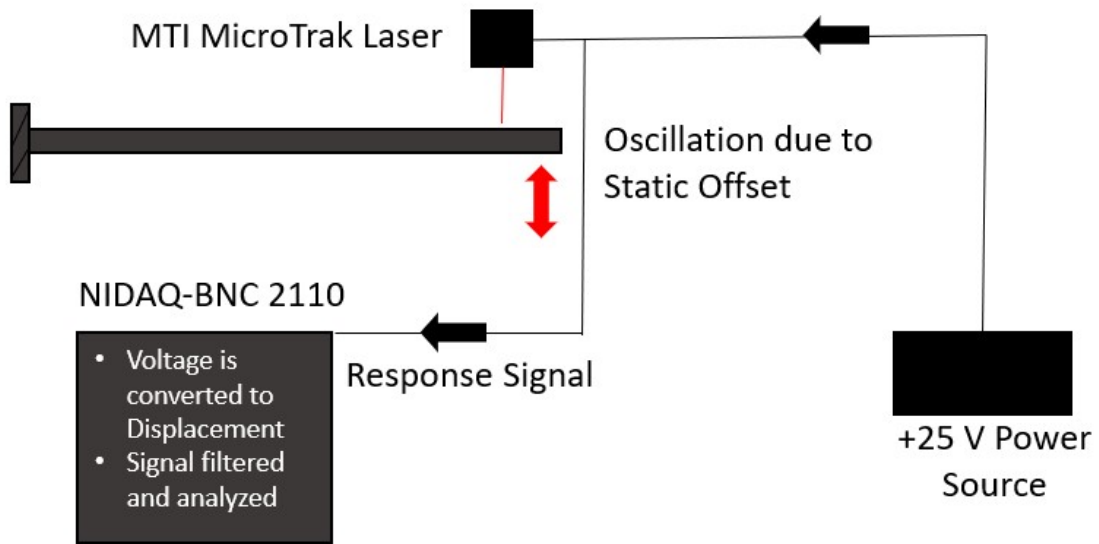


Figure 2.5: Beam Test Setup Simplified

2.4.1 Approach to Data Analysis

In order to extract damping ratio and other significant information from the voltage signal, the data is filtered with a 6 Pole butterworth bandpass filter (this cuts out noise coming from low frequencies). This is followed by a Hilbert Transform (applied via Matlab function) that produces an envelope around the sinusoid, tracking overall signal amplitude till the signal decays. The Log Decrement, typically used as a rough estimate of damping ratio in sinusoidal signals, is implemented repeatedly along the duration of the envelope, producing a weighted value for Damping Ratio (λ). This λ will be a measure of fitness for each damping treatment. The damping ratio outputs are plotted in bar graphs and then analyzed from there. The progression from Data Acquisition to generating images is succinctly captured in Fig. 2.6.

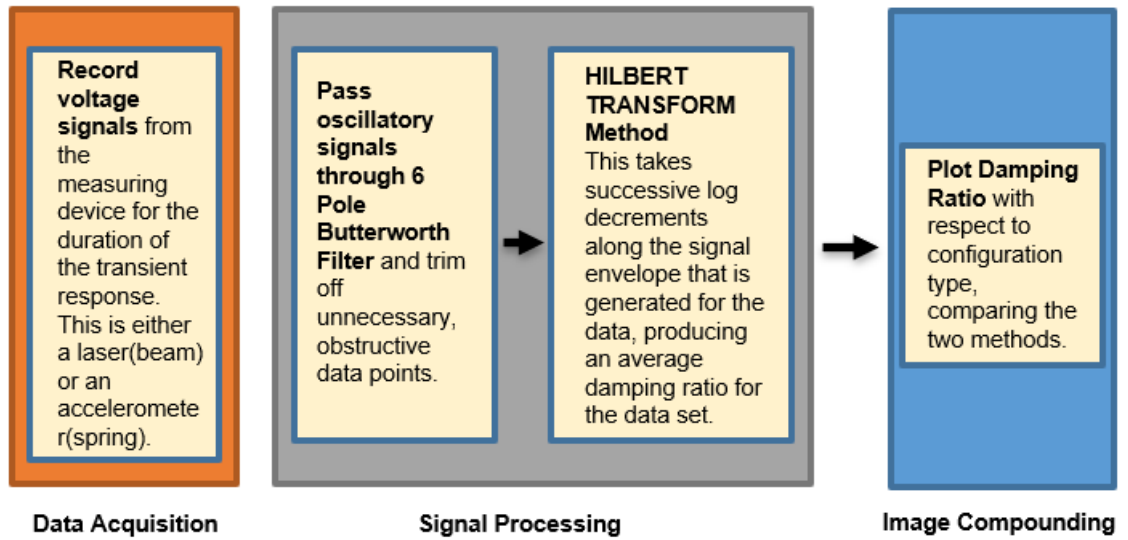


Figure 2.6: Approach to Data Analysis

2.4.1.1 Log Decrement Ratio

The Log Decrement Ratio is a damping estimate that is calculated using consecutive peak amplitudes within a diminishing, oscillating signal. A detailed explanation is contained in Appendix B.

2.5 MJM Test Results

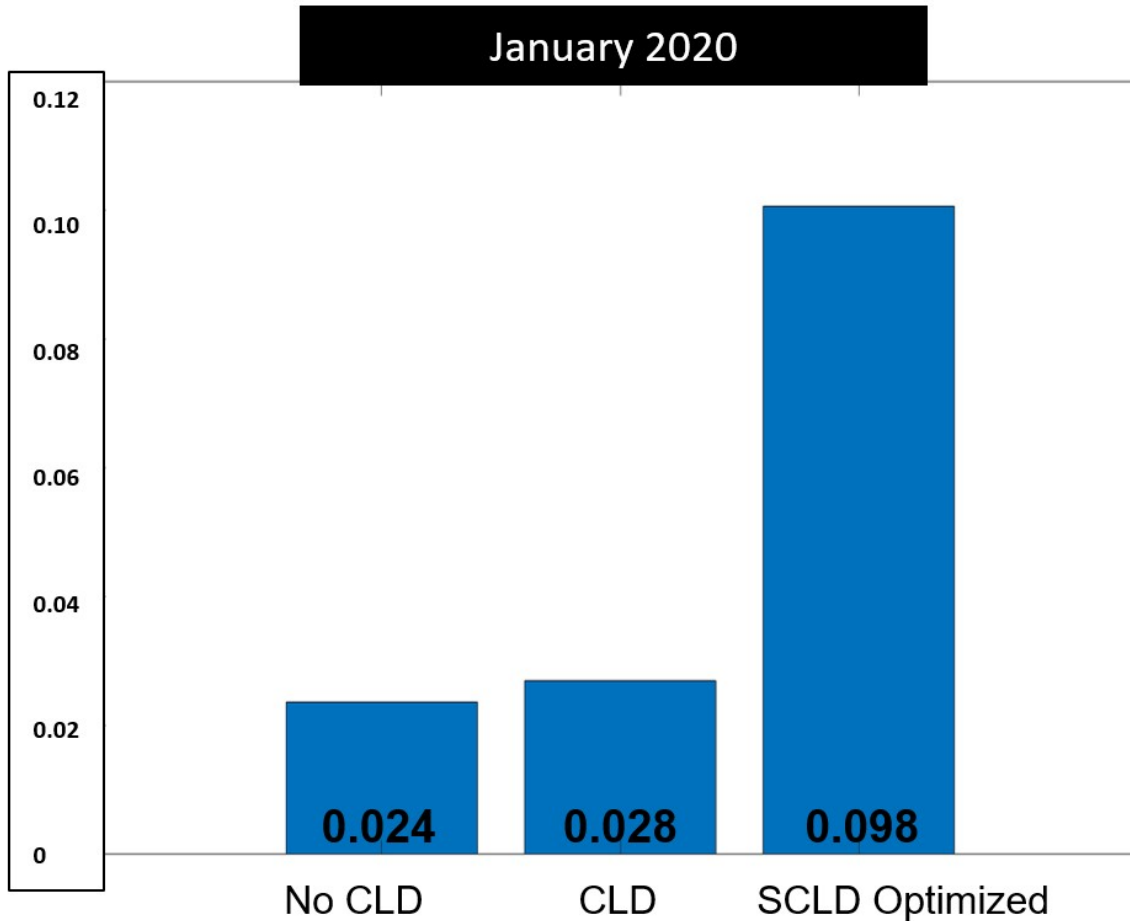


Figure 2.7: MJM Beam Damping Ratio Histograms (Transient Response)

Fig. 2.7 contains the first set of damping ratios captured from the MJM Beams. Over the course of the following 7 months, two more tests were taken and comparisons done in order to test the materials for temperature dependence. Due to the beams continuing to cure when exposed to ultraviolet light and a stark difference in temperature between the test dates, there was a concern that the beam would not respond in a consistent fashion.

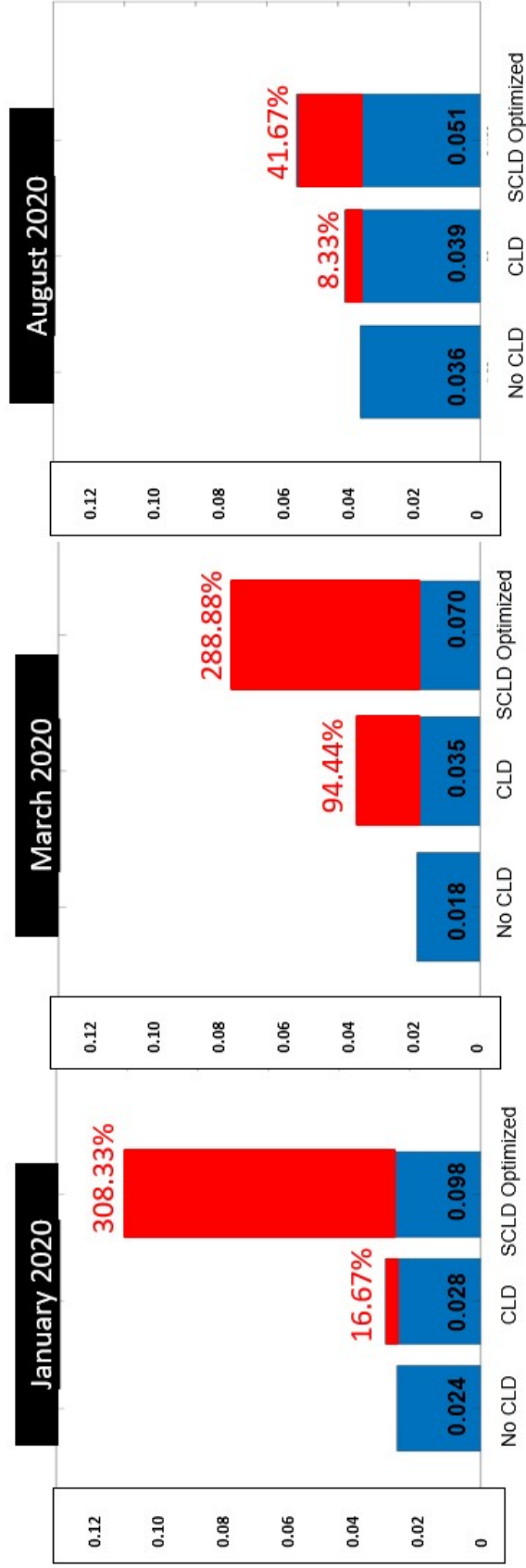


Figure 2.8: Comparison between January, March and August Damping Ratios for MJM Beams RED indicates percent increase in damping from the Untreated case.

The red sections in Fig. 2.8 are meant to highlight increases in damping with respect to the untreated case. Table 2.2 lists the percent increases and helps to illuminate the large changes in damping ratio from month to month.

Test Date (2020)	CLD	SCLD Optimized
January	16.67	308.33
March	94.44	288.88
August	8.33	41.67

Table 2.2: Percent Increase in Damping Ratio amongst MJM Beams

2.6 Conclusions

It is clear that the CLD and SCLD Optimized configurations are very effective, as damping ratio were not only always positive but increasing by up to 300 percent in one case. However the material properties were not reliable as they are known to change dramatically with temperature and with this study appear to change over time. This means that damping treatments made with this technology can not be trusted to reproduce performance measures if the temperature is not kept constant across test periods.

There is a need to find how CLD beams can be constructed and tested without the convenient "print all at once" approach.

2.7 Fused Deposition Modeling

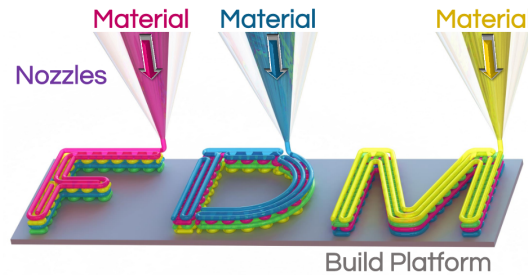
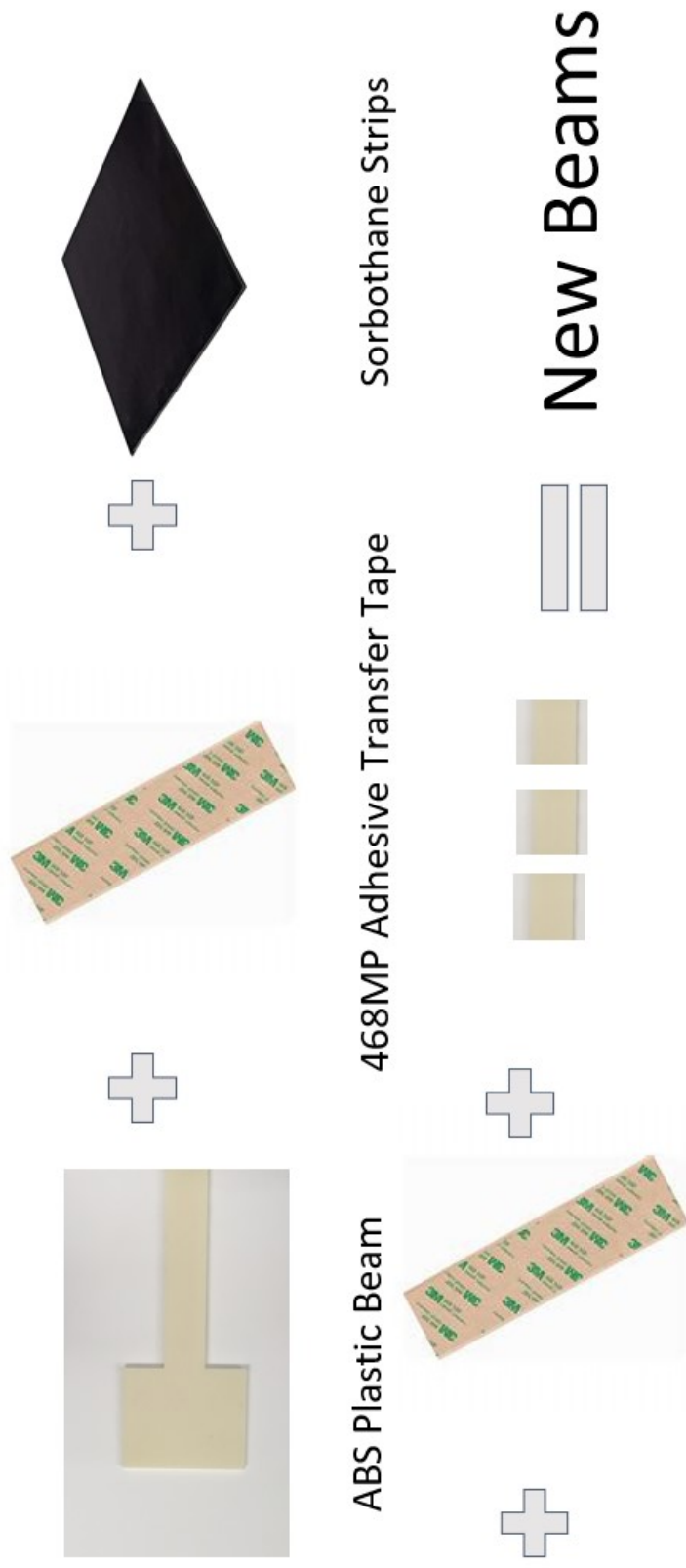


Figure 2.9: Fused Deposition Modeling Graphic

Fused Deposition Modeling is a form of additive manufacturing that involves the stacking of layer upon layer of very hot, extrudable material upon a build plate. Each layer (like depicted in Fig. 2.9) is solidified as it cools, so that another layer of material can be laid. This method of additive manufacturing is beneficial because of its high resolution, and because of its material versatility. FDM can reach resolutions of 0.25 millimeters, and print materials that are as stiff and brittle as tough plastics. With this capacity, samples can be generated at a surprising rate at high accuracy. Complex shapes can be generated in 3D modeling software that would have otherwise been machined or painstakingly glued by hand. This allows for more creative ideas and prototyping of how the treatments and structures discussed in this research can be applied. The Stratasys uPrint SE Plus employs a print bed volume of $200 \times 200 \times 150 \text{ mm}^3$ and is capable of printing batches of samples within a few hours. The period spent waiting, unlike in most other research processes, can be spent on analyzing data, forming new hypotheses or other relevant actions besides machining new parts. Particularly when dealing with adhesive damping materials

that have to be applied carefully to surfaces, so that the layers align and will not fall off, the ABS plastic used in the Stratasys uPrint machine is very serviceable. The 3D printing improves recurrence and efficiency in the research process, and precision of the treatment geometry, while allowing for material versatility.



ABS Plastic Beam 468MP Adhesive Transfer Tape Sorbothane Strips

New Beams

Figure 2.10: Example of fused deposition modeling and hand-layup process

2.8 FDM Material Properties

For the method of construction involving FDM printers, intermediate layers were added to the traditionally 3 ingredient recipe:

- Base Beam Layer
- Viscoelastic (VE) Layer
- Rigid Constraining Layer
- Adhesive Tape

In the following sub-sections the materials used to represent these essential components are described and supported as to which needs they meet and why.

2.8.1 ABS Plastic

ABSPlus is an ABS plastic based compound that maintains most ABS material properties, while warping less in response to heat [23]. It plays the parts of beam material and constraining layer material for this research, but its function as a constraining layer is of primary significance. A constraining layer must be tough enough to resist the vibration of the VE layer it's attached to, without being so heavy that it shears off when the surface shakes at or near resonant frequencies [5].

2.8.2 Sorbothane

The elastomer used displays low transmissibility (amplification) at resonance, demonstrating damping superiority [24]. The material is readily available and low-cost, making it ideal both financially and in the engineering sense, for this research. It is classified as viscoelastic in this research because of its ability to distribute force in many directions and deform freely under load, while returning to its original shape after deformation. It is applied by hand using adhesive tape, for the purposes of this research.

2.8.2.1 3M 468 MP

At the professional recommendation of sorbothane manufacturers, an industrial grade 0.1 mm adhesive transfer tape was used to bind all primary layers together, ensuring that each beam would be tightly bonded, strong enough in shear to provide useful data without falling apart. The tape is and applied by hand after cleaning the plastic beam and VE layers with professional grade propylene glycol. As seen in Table 2.3, the material does not have measured values for tensile and shear moduli due to its thinness.

Materials	Young's Modulus (MPa)	Shear Modulus (MPa)
ABSPLUS	2200	814.8
Sorbothane	91.00	30.54
468MP Adhesive	N/A	N/A

Table 2.3: FDM Beam Materials

2.9 Configuration Designs

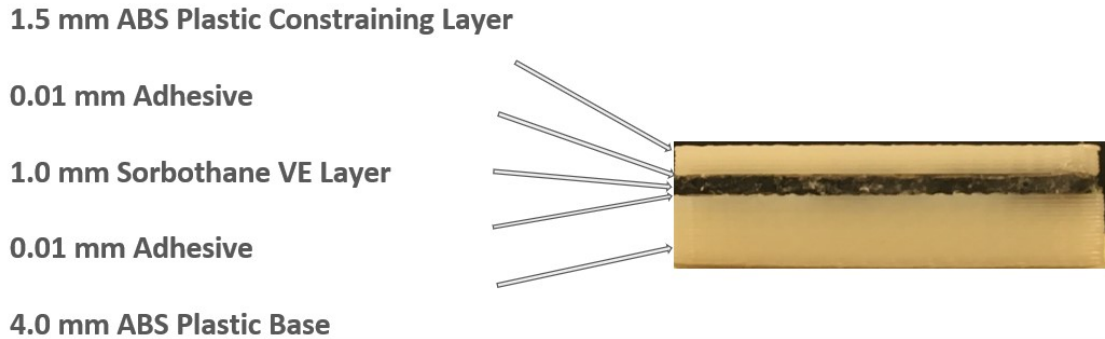


Figure 2.11: SCLD Treatment Layup

Fig. 2.11 above shows a front view of what the generic FDM treatment layup looks like for this research. The layers are manually applied using the adhesive tape as a binder. Chapter 1 provided background to the idea of testing different variants of the SCLD method in order to compare with optimization methods recommended in past research. The following subsections describe each configuration and how they were built. The major difference dimensionally between the FDM beams and the MJM beams is that the beam length had to be shortened to 101.6 mm (or 4 inches), so that the beam footprint could fit on a Stratasys uPrint build plate. No other dimensions were altered, even after noting that the beam would no longer be as slender, so that as much similarity between the application of two beam configurations (FDM and MJM) could be preserved.

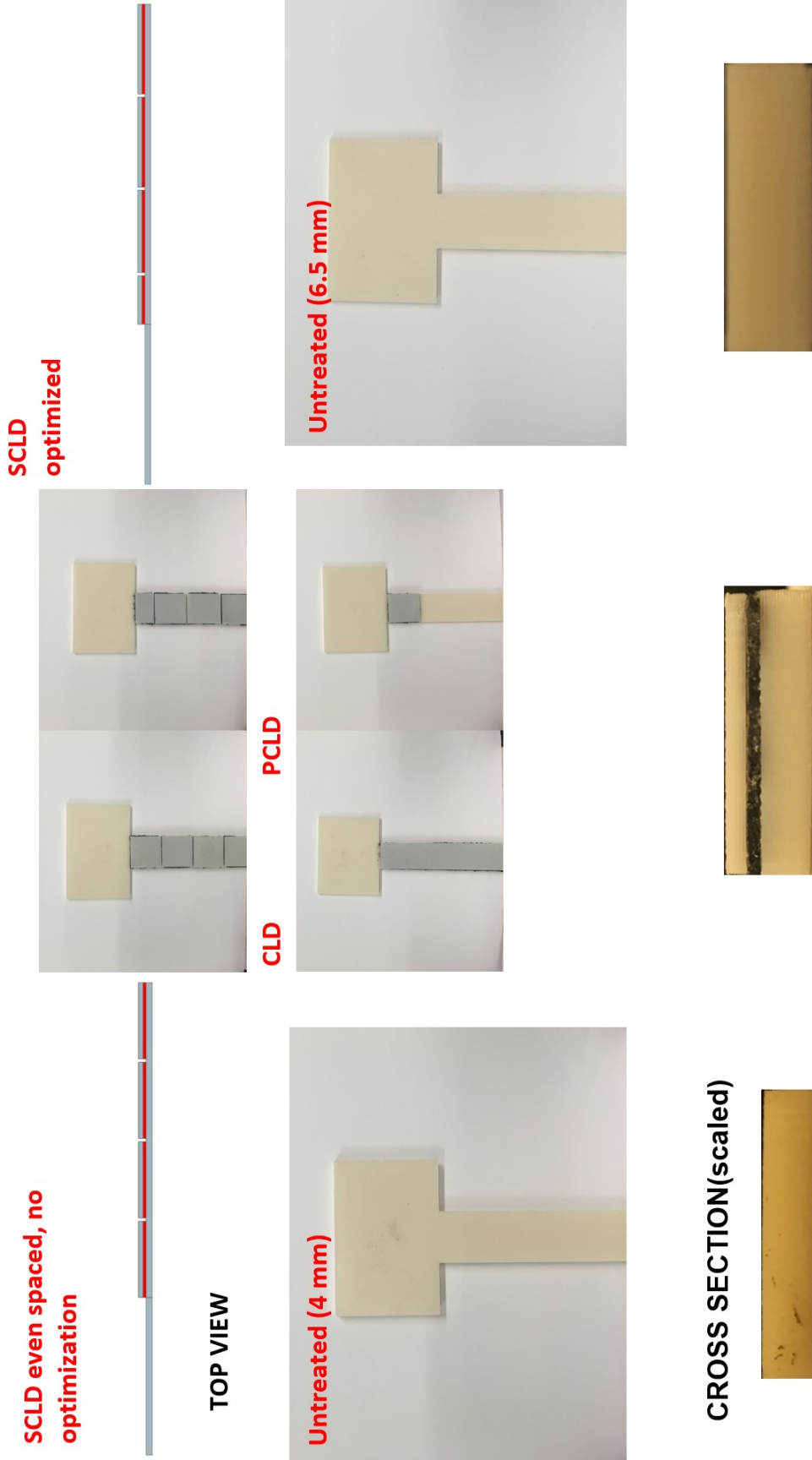


Figure 2.12: Cantilever Beam Configurations (top view and cross section)

2.9.1 SCLD Even Spaced Beam

In addition to the three primary configurations, the SCLD Even Spaced Beam was conceived as a foil to the SCLD Optimized beam. The even spaced beam has the same number of cuts, except they are evenly spaced across the 101.6 mm length. This hopefully will provide more information about the effectiveness of the SCLD optimized beam as a truly optimum configuration.

2.9.2 Partially CLD Beam

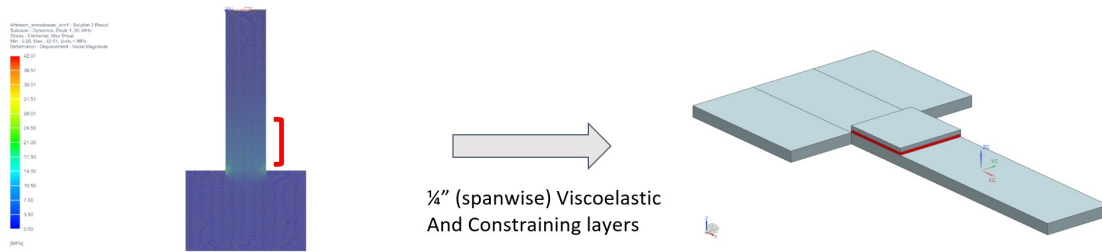


Figure 2.13: PCLD Beam Conception

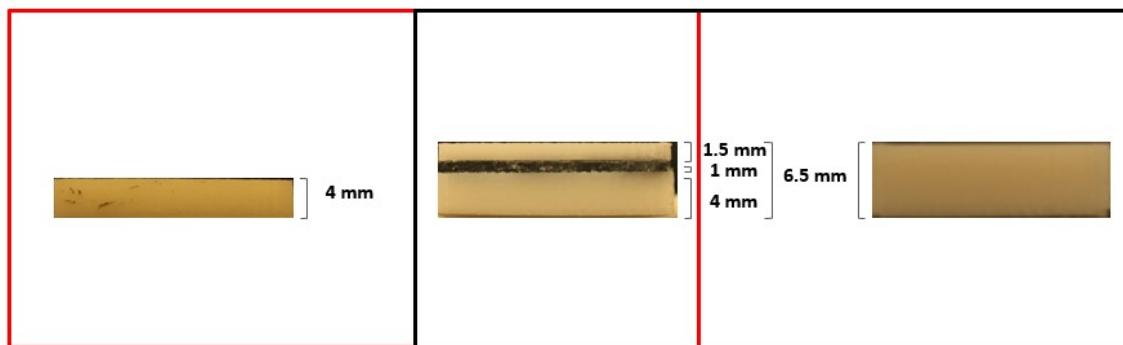
The Partially CLD (or PCLD) beam is based on modal analysis done on a model made with Computer Aided Design software. Shear Stress distribution was taken for the first mode and used as a basis for placing a constrained layer. Fig. 2.13 indicates where the max shear stress is predicted to appear when the beam vibrates in it's primary mode, and the partial treatment of the beam surface is the reason for the PCLD label. The finite element analysis was made to output 10 modes, with the mode carrying the highest weight in the Z direction (mode 1) being selected for the stress analysis.

2.9.3 Thicker 6.5 mm Beam

A thicker, untreated beam was printed from ABS Plastic so that certain design scenarios could be compared experimentally. The original untreated beam is 4.0 mm, and all the damping configurations are 6.5 mm thick. The plain 6.5 mm beam is intended to contrast with these two other categories of beams so that two different approaches to design can be assessed. Fig. 2.14 separates visually the two scenarios as:

- Considering adding damping to an existing surface.
- Designing a damping treatment to fit within a constrained volume/thickness.

This can expose situations where the damping treatments are especially effective.



- Adding a damping treatment to an existing surface
- Designing a treatment layer within a constrained volume

Figure 2.14: Two Design Scenarios Compared

2.10 Test Results

The materials used in the FDM construction process all maintain their properties despite changes in time and temperature, and so seasonal test updates are not provided here, as data did not fluctuate.

Damping Ratios were plotted in bar graphs, per scenario, and then overall. Similar to the results from the MJM tests, the CLD and SCLD Optimized beams paced the field. The only two configurations to show an increase in damping ratio with respect to the untreated beam increased by **74.07** (CLD) percent, and **18.5** (SCLD Optimized) percent. Unlike the previous data, the SCLD Optimized beam did not have the highest increase in damping ratio, foreshadowing possible errors in either testing, manufacturing, or the hand-layup assembly process.

The focus when analyzing these values is placed on the percent increase in damping, rather than the values themselves, due to the vastly different material properties between the two types of beams (MJM and FDM).

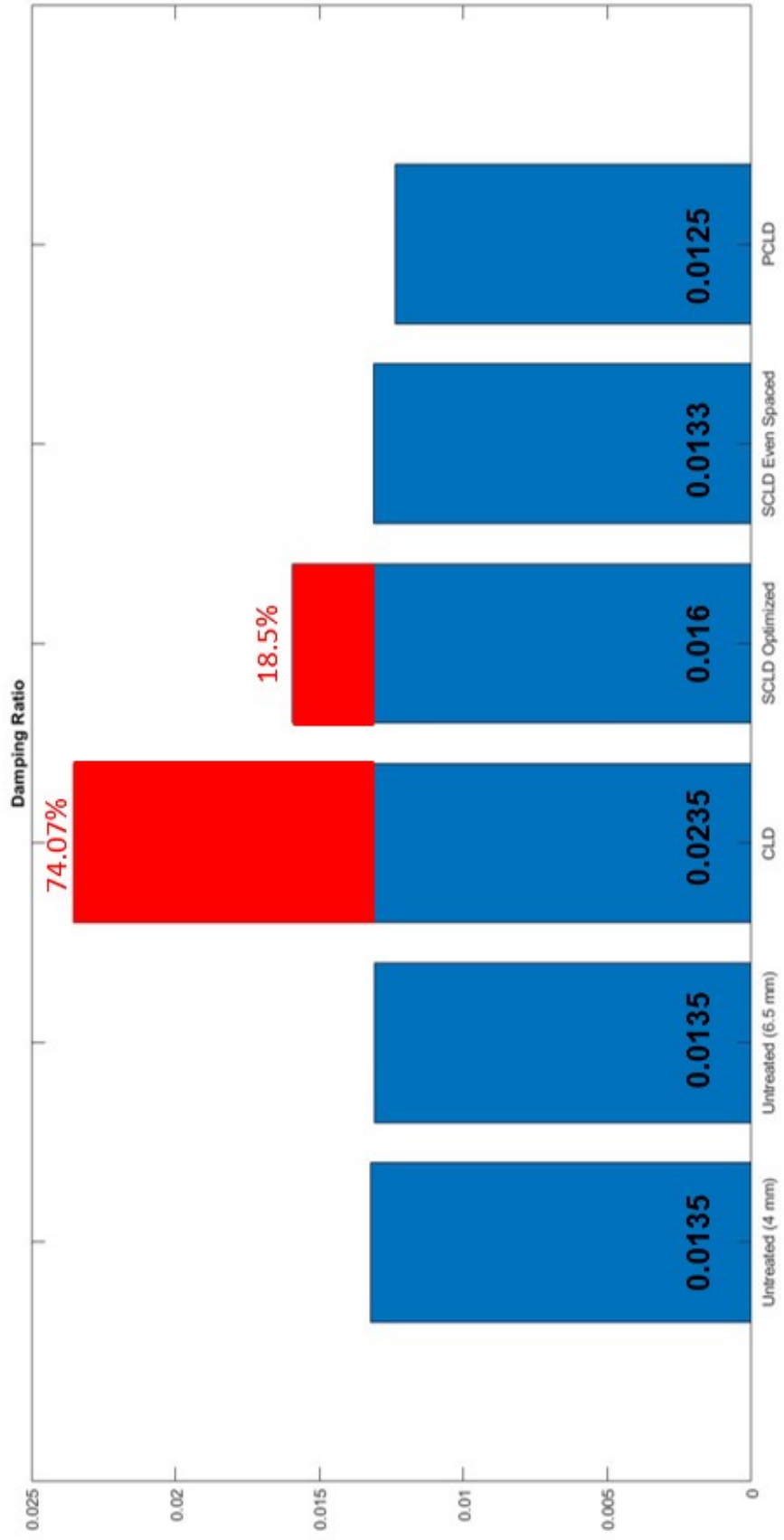


Figure 2.15: FDM + Hand-layup Damping Ratios (Transient Response)

2.11 Conclusions

Fig. 2.15 only the CLD and Optimized SCLD beams were shown to increase damping, but the optimized method was severely outperformed. The beams printed wholly with MJM, although compromised by changing properties, saw higher damping ratios and percent increases in damping for the CLD and SCLD treatments.

Fig. 2.16, and Fig. 2.17, show side views of two kinds of 3D printing methods that were utilized. The roughness in construction for the FDM process is visible, and is certainly a contributing reason why the maximum FDM damping ratio ($\lambda = 0.0235$) is almost an order of magnitude lower than the maximum MJM damping ratio ($\lambda = 0.098$). Even with the massive decrease in MJM material properties, the results were not comparable. Potential sources of error in the FDM constructed beams might include:

- Bond strength between essential layers, and adhesive tape layers
- Foreign particles, air bubbles between layers

Overall we see that the MJM printed beams were largely without deformities or misalignment between layers, and the bonding between adjacent layers was consistent along the beam lengths. The structural excellence produced high damping values and large increases between the untreated beams and the optimized configurations. However the material high sensitivity to temperature, possibly combined with an ongoing curing process may limit widespread use. With the FDM beams there is a much longer life span for the samples due to materials that fully cure

when cooled, however there is much room for debris like hair and dust to pollute the laminate, and manual construction lends itself to misalignment even with a very careful eye.



Figure 2.16: Side View of a MJM SCLD Beam



Figure 2.17: Side View of an FDM SCLD Beam

Considering the scenario specific data, we see that when adding damping to a preexisting surface, or subtracting from a constrained area in order to maximize

space, high increases of damping may be possible. This is an important conclusion because 3D printing provides the opportunity to customize beam laminate cross sections with high detail.

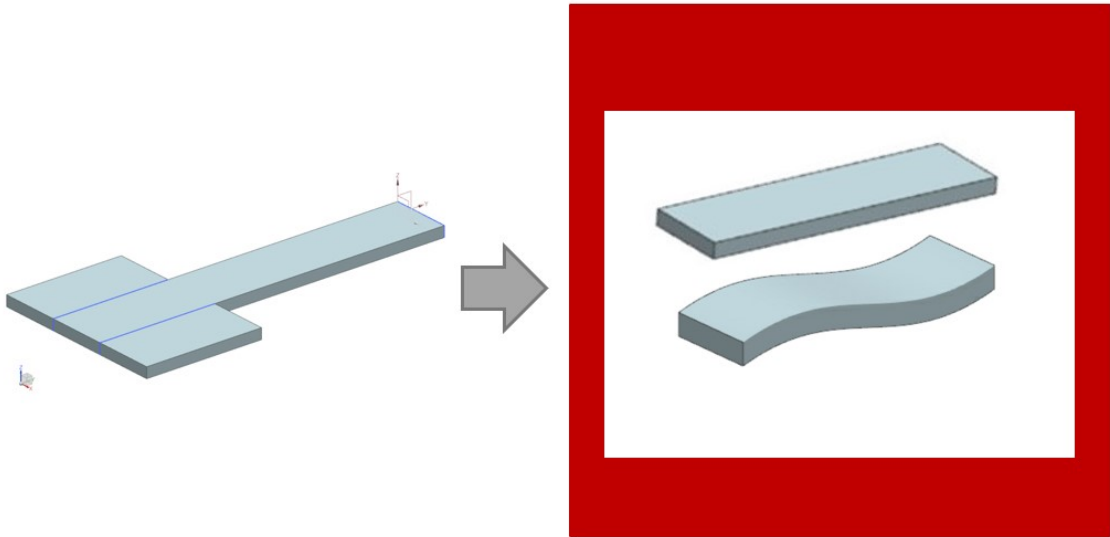


Figure 2.18: Using Structural Design to Increase Damping

It has been experimentally confirmed, with both fabrication methods, that the SCLD Optimized configuration is more or as effective than conventional ways of applying damping. This of course is highly situational, but still a promising result for the genetic algorithm that produced the model. The next chapter will experimentally test the effect of sinusoidal structures on not only the SCLD Optimized configuration, but all the damping treatments tested thus far.

Chapter 3: Damping Treatments for Sinusoidal Strut Springs

3.1 Beam Structure Overview

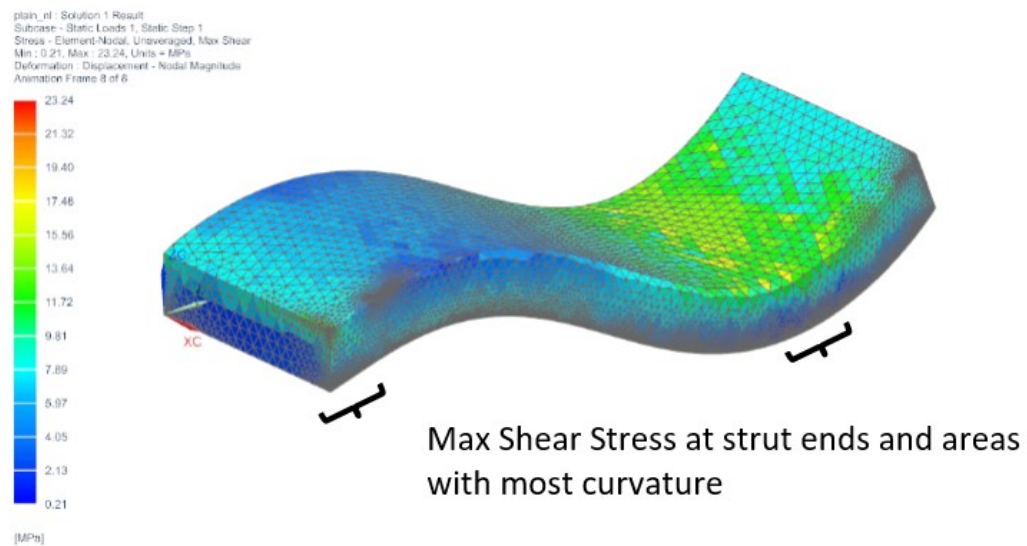


Figure 3.1: Shear Stress Distribution in Sinusoidal Beam

Recall that in Section 1.5, sinusoidal beams were briefly introduced as having the capacity to augment passive damping capabilities in a treatment. The idea is that changing curvature in the structures can induce more shear strain in the VE layer of damping treatments. Studies have already shown that shear deformation in the VE layer is premium when discussing CLD [25]. In this research, the sinusoidal

structures are conceptualized and experimentally validated for damping ratios in order to take advantage of this. The same damping treatments as were used on cantilever beams will be transferred over to these sinuous structures; this is so the effect of the curvature can be more properly isolated. In light of this, axial springs with rectangular cross sections that are initially straight and initially sinusoidal along their length will be used to test damping treatments. Fig. 3.1 shows more evidence to support the claim concerning the sinusoidal beam. The CAD beam is simulated through a static compressive test, and made to show where the shear stress is distributed along the structure as a result. It can be seen that the areas of maximum curvature display the highest shear stress. This is the founding principle expounded upon through experimentation in the following pages.

3.2 MJM Spring Sample Fabrication

The sinusoidal beam used to form the body of the spring is formed in the shape of the sine wave seen in Fig. 3.2. The exact shape of the sine wave is not essential for this proof of concept study, only that the curve is sinusoidal, with curvature that is periodic or balanced along the length. The length of 1 in. (25.4 mm) was derived from previous work on this shape [19]. The small size also made the springs ideal for attachment to the electrodynamic shaker platform.

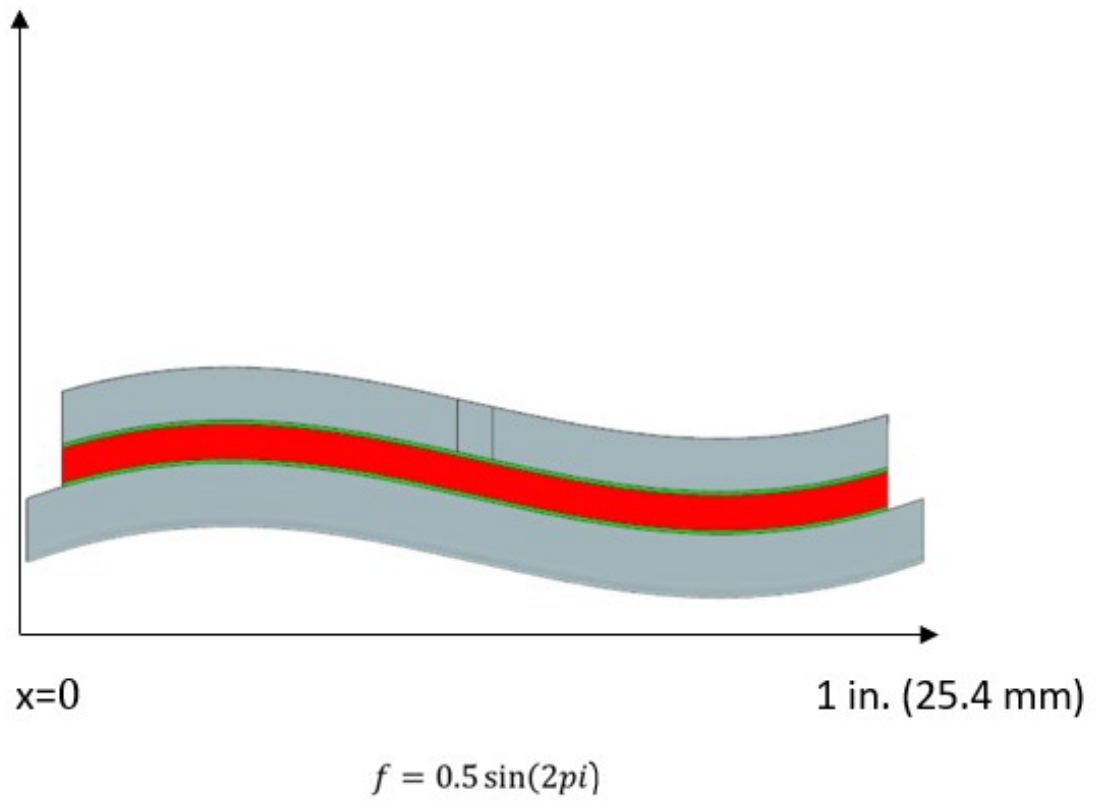


Figure 3.2: Sinusoidal Beam Wave Equation

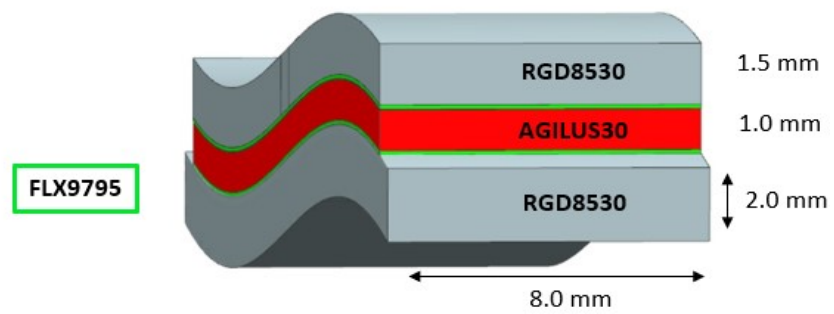


Figure 3.3: Sinusoidal Beam Layerwise Configuration

Fig. 3.3 highlights a major change to the basic dimensions of the "beam" portion of our damping treatments. Instead of a 4.0 mm beam base thickness, the base is 2.0 mm thick. This is a departure from the Guiding Assumption that led us to choose a beam base thickness of 4.0 mm for the cantilever beam tests. The research of Al-Ajmi and Bourisli (where the optimization dimensions for h_1 and h_2 were taken from) did not specify a required thickness for h_3 , so 2.0 mm was chosen so that the beam would remain slender (in proportion to the 25 mm length and 8.0 mm width) and so that the beams would not obstruct one another during vibration. Maintaining a 4.0 mm thickness would have required a much taller spring, which would complicate printing many copies of the spring, and attaching it to the shaker platform (only 4.0 inches in diameter).

3.3 Material Changes

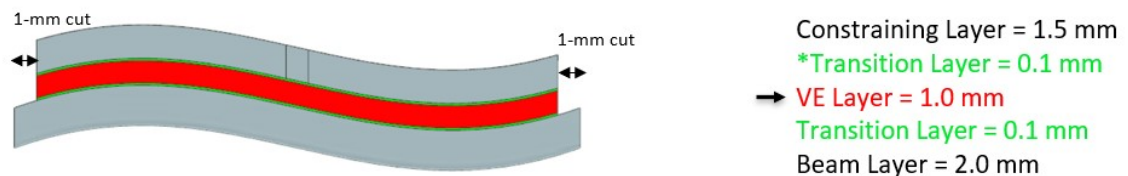


Figure 3.4: Sinusoidal Beam Laminate Composition

3.3.1 RGD8530

RGD8530 was used as a replacement material for VeroWhite in the beam base layers of each spring. This was done because RGD8530 responded much better to the heat that is required to push in brass heat set inserts (needed to attach test

articles to the electro-dynamic shaker) into the spring surfaces. The RGD8530 is still very stiff [26], producing the shear strains needed to augment the SCLD, but temperature rated so that it can be manipulated for testing. The hope was also that with a softer structure, there would be more axial displacement, and as a result more change in curvature and damping in the beam without reduced stiffness.

3.3.2 FLX9795 (Transition Layer)

The 1 mm cut width was kept the same from the cantilever beam SCLD approach. One major change in the laminate composition can be seen in Fig. 3.4. A new intermediate transition layer was added to the MJM and FDM versions of the beam laminate. For the MJM beam the transition layer is meant to produce a stiffness gradient between the very stiff base layer and the soft VE layer. For the FDM beam, the transition layer is not additive, but a label for the 468MP adhesive tape layer introduced in section 2.8. FLX9795 is a material that has a softness and Young's Modulus [27] that make it a better binder to both RGD8530 and AGILUS30. This change was made so that the bond between layers would be strong enough to allow for higher shear deformations in the VE layer. It has been shown in previous research that even small strains in bonding layers can have a significant effect on frequency dependent damping ratios [28] so even a small increase in potential here due to a change in material, can impact results greatly.



Figure 3.5: MJM Sinusoidal Spring Configurations

Materials	Young's Modulus (MPa)	Shear Modulus (MPa)
RGD8530	1400	571
AGILUS30	1.265	4.27
FLX9795	23.125	8.03

Table 3.1: MJM Spring Materials

The MJM Sinusoidal springs were treated with the same 3 initial configurations from chapter 1. The print time for one batch of three springs was about 2 days to account for not only printing but post-processing. It was important that the springs be printed horizontally so that the beams would have smooth surfaces and be strong in vertical deflection. The FDM Sinusoidal springs required more manual labor in lamination of the VE and constraining layers to the base structure. Fig. 3.6 highlights the materials used, and Fig. 3.7 highlights the additional changes required for springs of all categories and configurations, so that they could bear weight and be attached to the electrodynamic shaker. The need for a load bearing brass insert will be elaborated on in the next section, but the base captured in the figure was necessary so that all tested springs might be secured to the shaker. It is worth

noting that the base was also 3D printed using FDM technology.

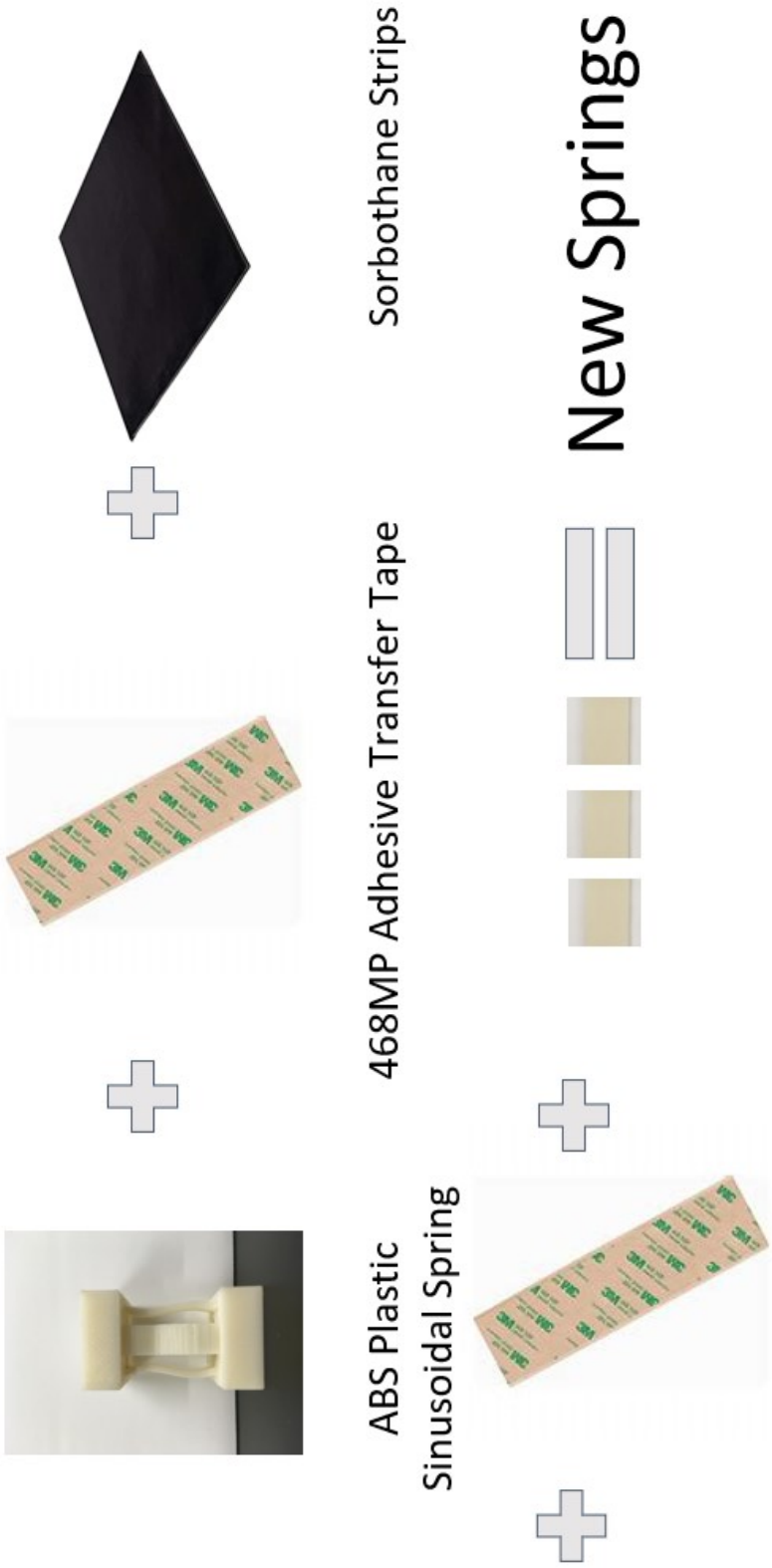


Figure 3.6: FDM Sinusoidal Spring Components

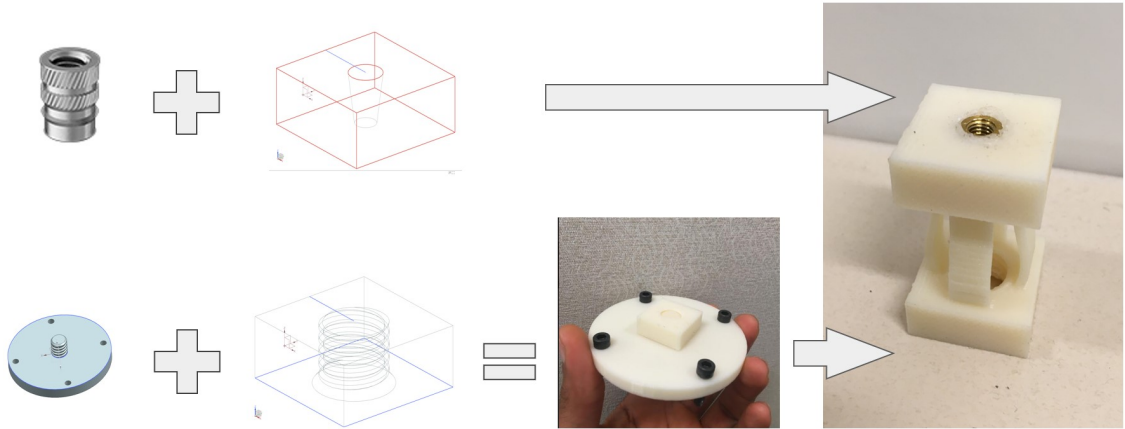


Figure 3.7: Modifications Required for Load-bearing and Attachment to Shaker

3.3.3 Rectangular Beam Spring

The Rectangular Beam spring was added as a foil to the Sinusoidal spring in order to isolate the effect of the sinusoidal structure on the various damping configurations used. The MJM beams and springs in the research were manufactured and tested in order to validate the damping methods, and so the variety of damping treatments, structural configurations seen (including the Rectangular Beam spring), did not become implemented until the FDM stage of the research. Results from Chapter 2 have already established the potency of both the traditional CLD, and the algorithm-generated SCLD treatment, and so reproducing the exact same test and samples for both printing types (knowing of the temperature sensitivity which leads to the property-creeping tendency of MJM) is redundant. The experiments of this chapter are meant to

- Test the SCLD optimized treatment for bending vibrations of a cantilever structure applied to axial vibrations of a sinusoidal structure

- Test the structure itself for effectiveness at increasing passive damping ratios

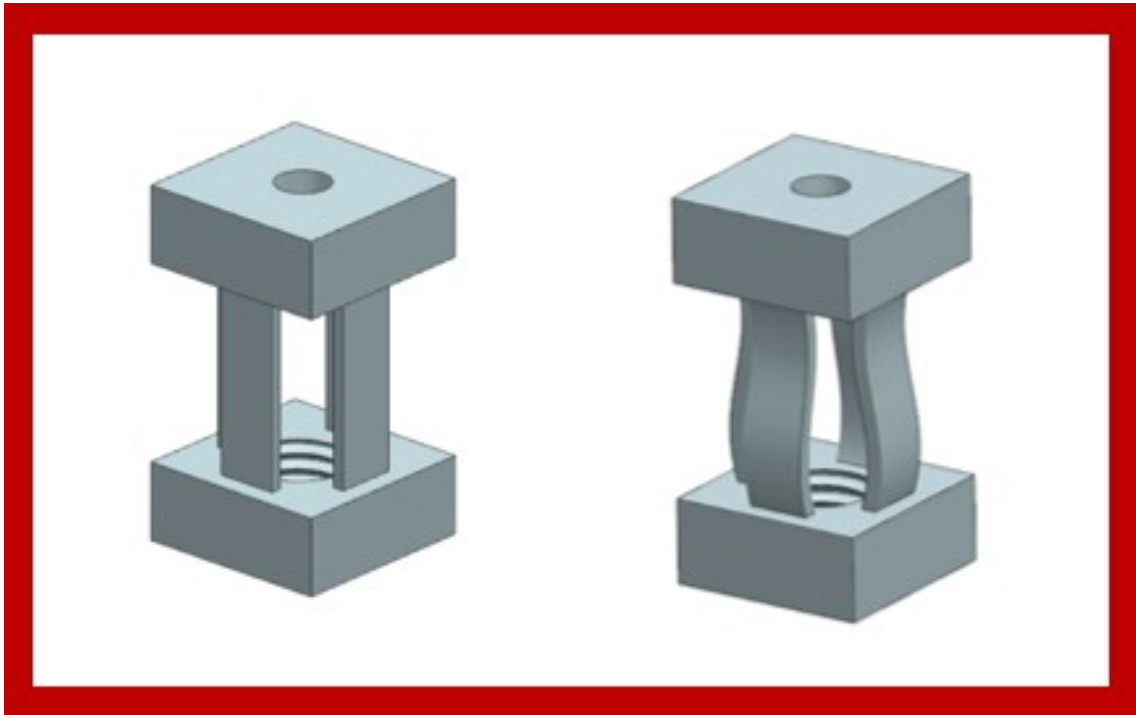


Figure 3.8: CAD Models of Rectangular and Sinusoidal Beam Springs

In Fig. 3.9 all configurations of the Sinusoidal spring, and their rectangular counterparts, are listed. The 50 mm high springs were made by cutting small pieces of adhesive tape and sorbothane, and applying them by hand to the 3D printed springs as each configuration required. The only configurations that differ from their cantilever beam versions were the PCLD configurations for the Rectangular Beam and Sinusoidal springs.

3.3.4 PCLD Rectangular Beam Spring

For the PCLD RB Spring, Fig. 3.9 shows that the patches of constrained VE material were placed at either end. This imitates the PCLD cantilever beam

configuration, where the area of max shear stress in the primary mode of vibration was covered. This stress-based approach was the basis for placing a PCLD patch at either end where there is expected to be maximum shear stress.

3.3.5 PCLD Sinusoidal Spring

Because the PCLD design is aimed at addressing areas of maximum shear stress distribution, and stress distribution is largely affected by structural design, this Sinusoidal Spring has a very different looking PCLD configuration than it's Rectangular Counterpart. Recall Fig. 3.1, where the image shows areas of max shear stress at the peaks of the sine wave structure. It is at these peaks that the corners of the damping patches end for this particular configuration. This is so the highest shear strains will occur at the free ends of each damping patch. Other than the two aforementioned springs, all damping configurations are the same across both structural categories.

Materials	Young's Modulus (MPa)	Shear Modulus (MPa)
ABSPLUS	2200	814.8
Sorbothane	91.00	30.54
468MP Adhesive	N/A	N/A

Table 3.2: FDM Hand-layup Spring Materials

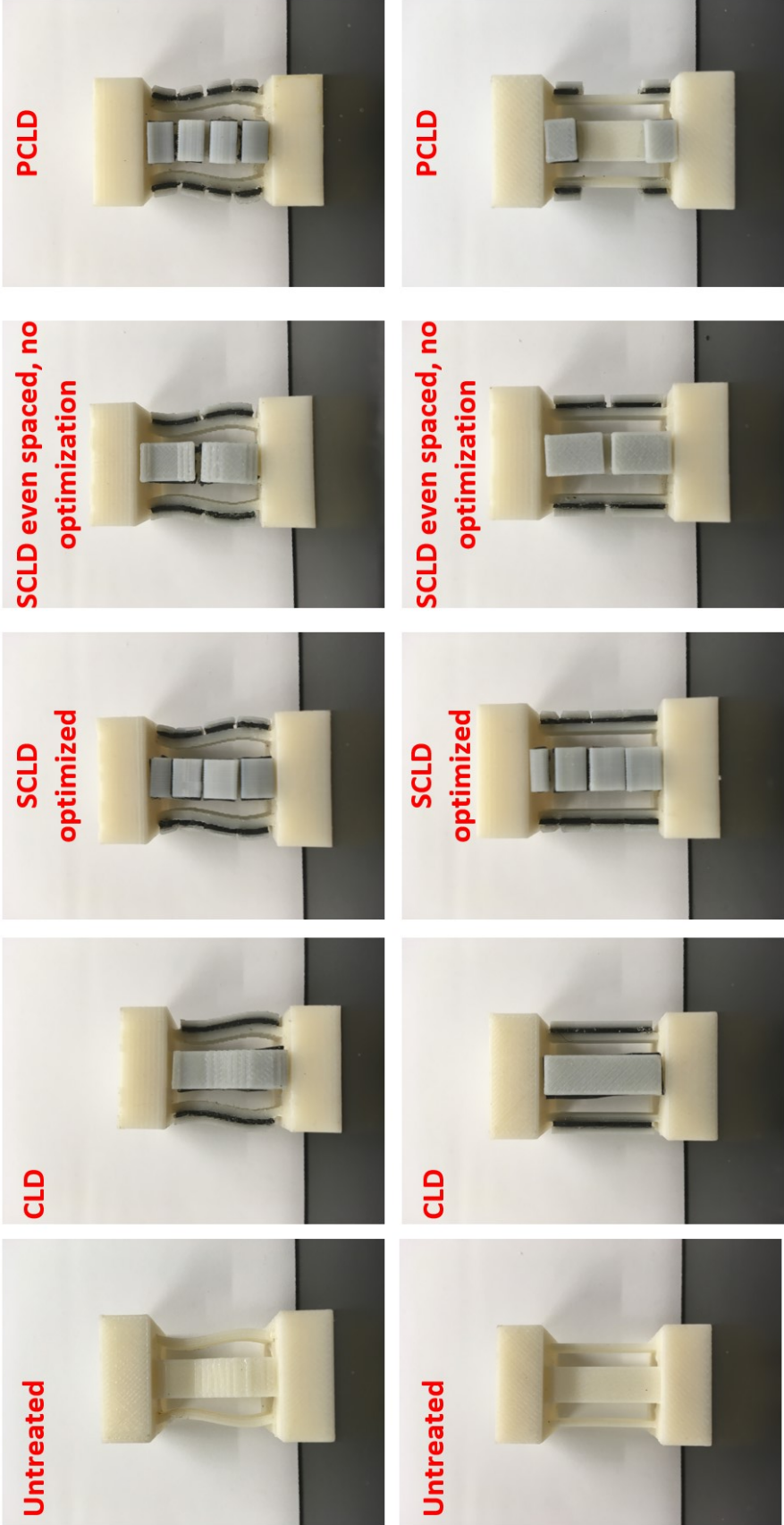


Figure 3.9: FDM + Hand-layup Spring Configurations

3.4 Spring Test Setup

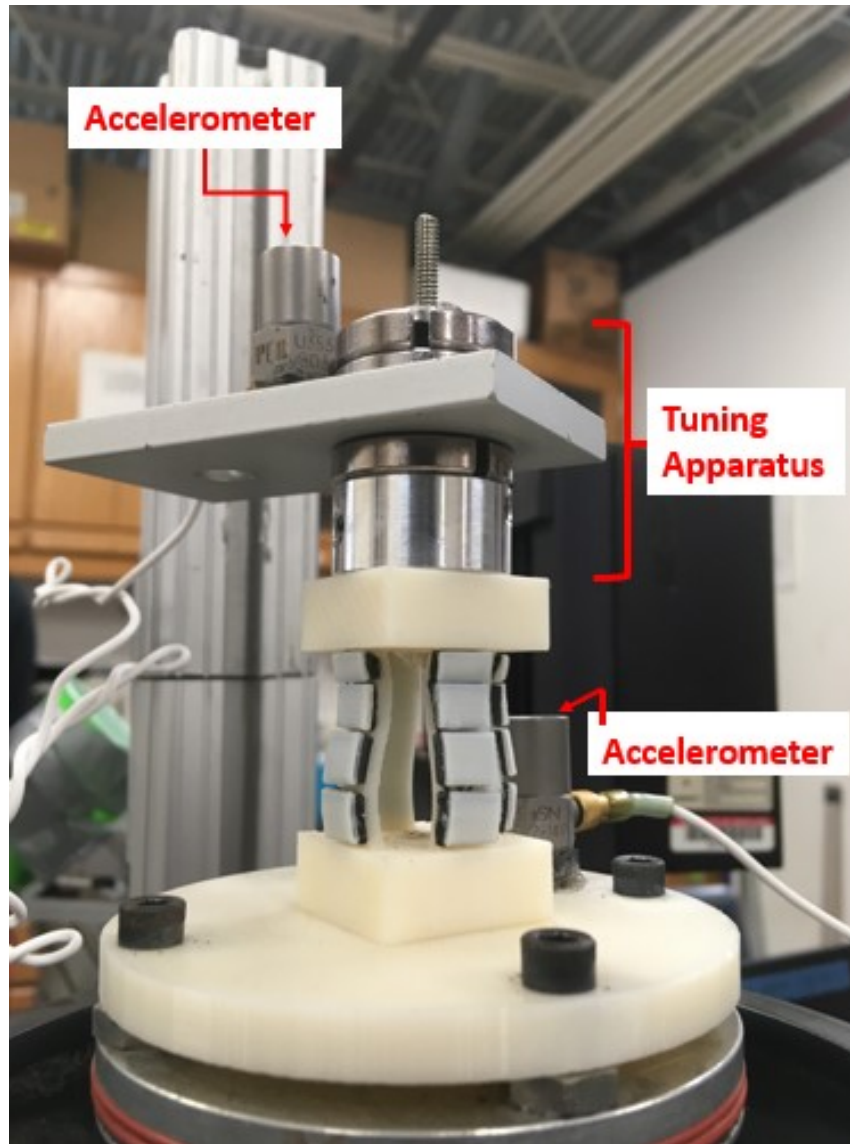


Figure 3.10: Electrodynamic Shaker Test

Above in Fig. 3.10, there are several things to note. First is the switch from analog lasers to accelerometers for measuring voltage. The accelerometers here offered higher resolution and sample rate than the lasers, which is needed for devices that are being driven at much higher frequencies. This segues into the next object

of note in the image. Atop the spring pictured is a contraption made of several weights. The weights are threaded to the spring via the brass heat insert at its top. The purpose of the weight (45g) is to place the fundamental frequency of each spring in a (lower) range that is easier for the electrodynamic shaker to function at [29]. Lower test frequencies also make sampling the output signal much easier. Recalling the basics of harmonic motion:

$$w_n = \sqrt{k/m}$$

where w is fundamental resonant frequency, k is axial stiffness, and m is mass loading of the spring. From this equation we see that raising m will decrease the fundamental frequency. Each spring's frequency was solved for by measuring static stiffness with a mechanical testing machine. The weight was then used to place the fundamental frequencies under 500 Hz. This was only an estimate at the **static** fundamental frequencies however, as the complex structures proved to make dynamic frequencies hard to pinpoint. Modal frequencies and charts varied from material to material (between 150 and 350 Hz).

The electrodynamic shaker was hooked up to a 25 V power supply and an amplifier that was used to scale the driving amplitude of the input signal. The two accelerometers trace back to a National Instruments data acquisition system which in turn was connected to a computer using SignalExpress to record and analyze the output signal. All tests were ran at an amplitude of 500 mV, which translates to roughly 1.25 mm [29] peak to peak displacement of the shaker. After each test the

spring was replaced, with the only (barely) changing variable being the tightness with which it was screwed into the base plate on top of the shaker.

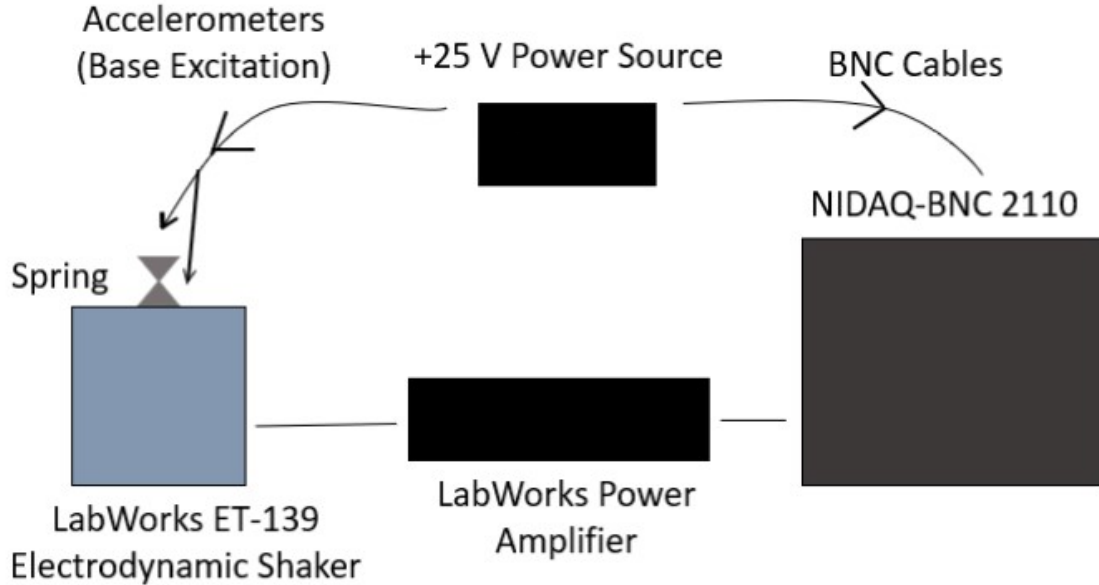


Figure 3.11: Spring Test Setup Simplified

The accelerometers convert acceleration (g's) into units of volts with 1 g of acceleration producing 10mv of output from the accelerometer. Before finishing each test, the acceleration array is divided by a value of $(w_n)^2$ (taken from the resonant peak in the output signal, see Fig. 3.13) to convert the accelerations into displacements. This conversion factor comes from the equation of motion convention that states that acceleration is the second derivative of displacement. Then SignalExpress is used to take both the input base excitation and response, and produce a transfer function representing the output magnitude with respect to one unit of input. These transfer functions are also known as transmissibility ratios, expressing how much of the input signal is transferred to the top of the spring from the base. The transmissibility ratios/transfer functions are then plotted with respect to

frequency in order to understand how the sample responds to base excitation in a certain direction.

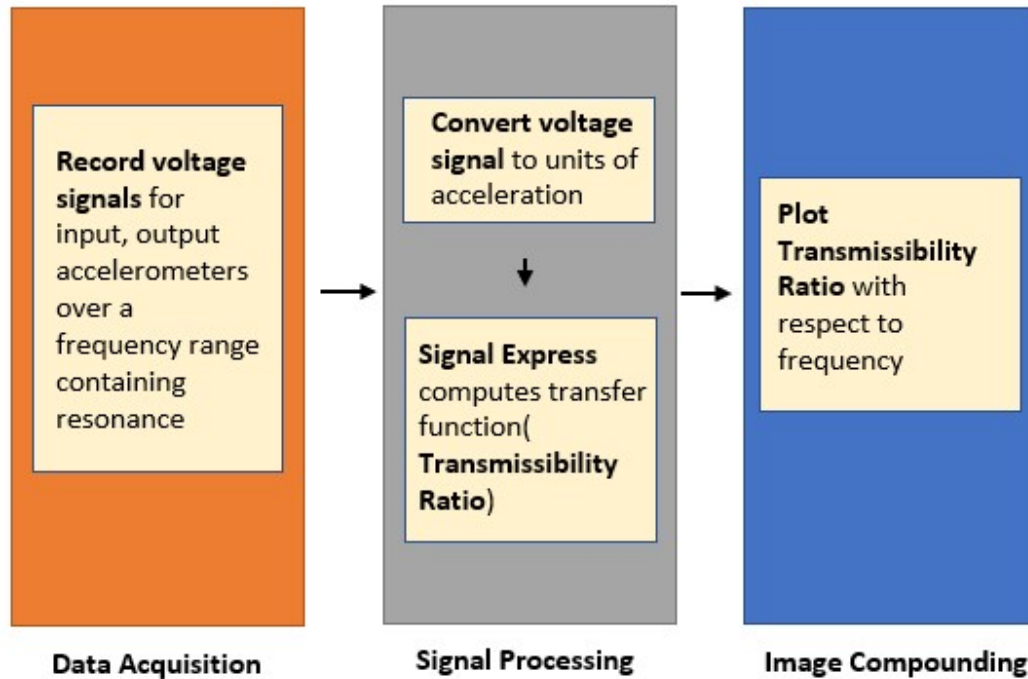


Figure 3.12: Approach to Data Analysis

3.4.1 Steady State Response Test

The steady state response test for the MJM springs was done over a frequency range of 200-500 Hz. The FDM Springs first three modes were located in a frequency range of 150-350 Hz. Fig. 3.13 shows an example of the transfer function generated for an MJM Sinusoidal spring. This function is used to compute damping ratio and to better understand how the structure operates dynamically. The Half Power Method (to be discussed shortly) is used to estimate damping ratio. The clear peak shown in the image is an indicator that there is a fundamental or resonant frequency at that point, and this provides basis for the transient test.

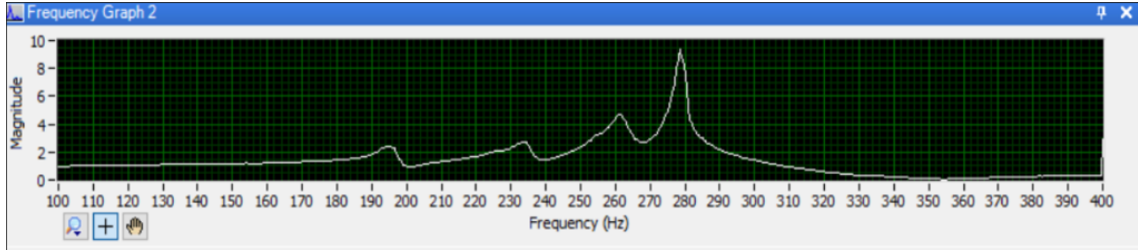


Figure 3.13: Example of Steady State Response Test for 1st Mode of an MJM Sinusoidal Spring

3.4.2 Transient Response Test

The steady state test helps you confirm what the fundamental or resonant (referring to any mode) frequencies are in a frequency range. When this is confirmed the samples are then driven at their resonant frequencies and released (see Fig. 3.14), the decaying vibrations are collected as transient data that can also provide information about the damping ratio. The Hilbert Transform is used again here to extract a damping ratio from each transient response signal. These two tests are used to generate data and compared to one another in order to validate conclusions about damping ratio and sample performance.

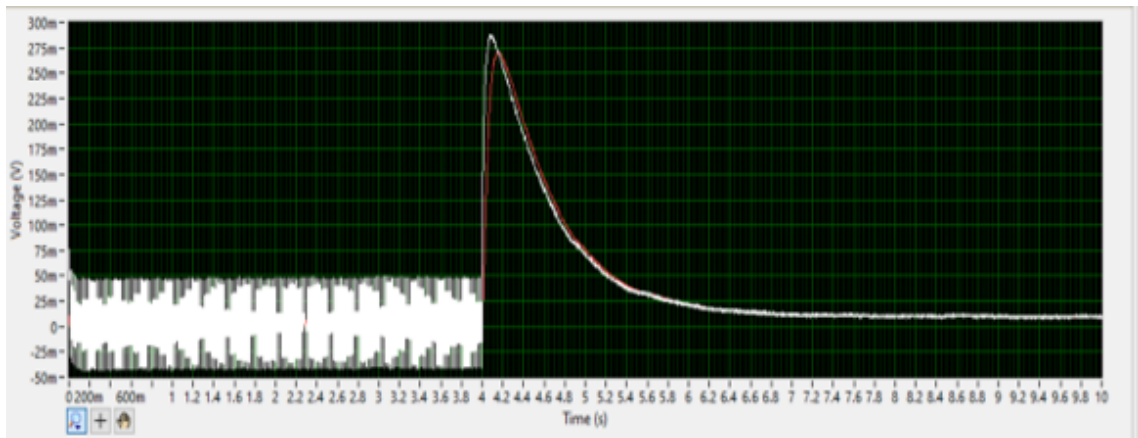


Figure 3.14: Example of Transient Response Test for 1st Mode of an MJM Sinusoidal Spring

3.4.3 Half Power Method

The Half Power Method is used in this chapter to numerically extract damping ratios from transfer functions. It has a high accuracy for damping ratios ≤ 0.05 . The formula is explained clearly in Appendix B.

3.5 Test Results

3.5.1 MJM Temperature Effects

Similar to the MJM beam samples tested in Chapter 2, performance change with respect to temperature is observed in the three damping configurations applied to MJM springs. Figs. 3.15, 3.16 and 3.17 help show the stark contrast between steady state response data taken in March and data taken in August 2020. It is clear in all three plots that there is a significant change in the shape and amplitude of the transfer function for samples made with these materials. Like before, the samples sensitivity to temperature caused properties to change, making this data unreliable in the long term. In the colder months (January, March) the samples stiffened and damping ratio increased. As the seasonal temperature increased, so did the relative change in damping ratio decrease. In spite of this, it can be seen in Figs. 3.18 and 3.19 that the CLD and SCLD configurations both were very effective in the initial stages of the sample testing. Tables 3.3 and 3.4 organizes the percent increases from both test so that a downward trend is more easily noticed as the samples age. Once again, we can see the effectiveness of the multi-jet modeling

technology at printing damping treatments, but there is not enough information to make any conclusions about the structure. The following results help solve this problem.

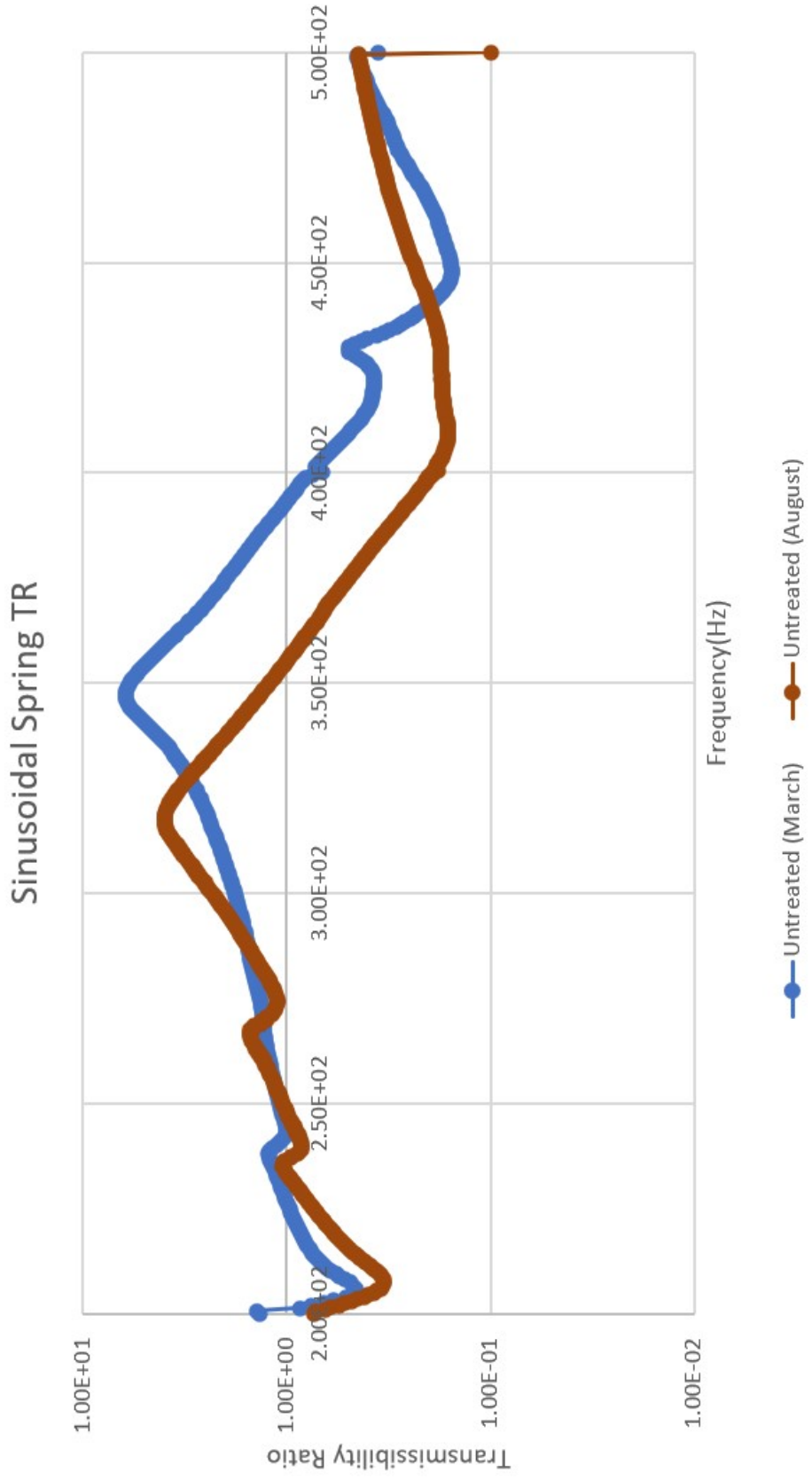


Figure 3.15: Untreated Spring Transfer Functions taken 5 Months Apart

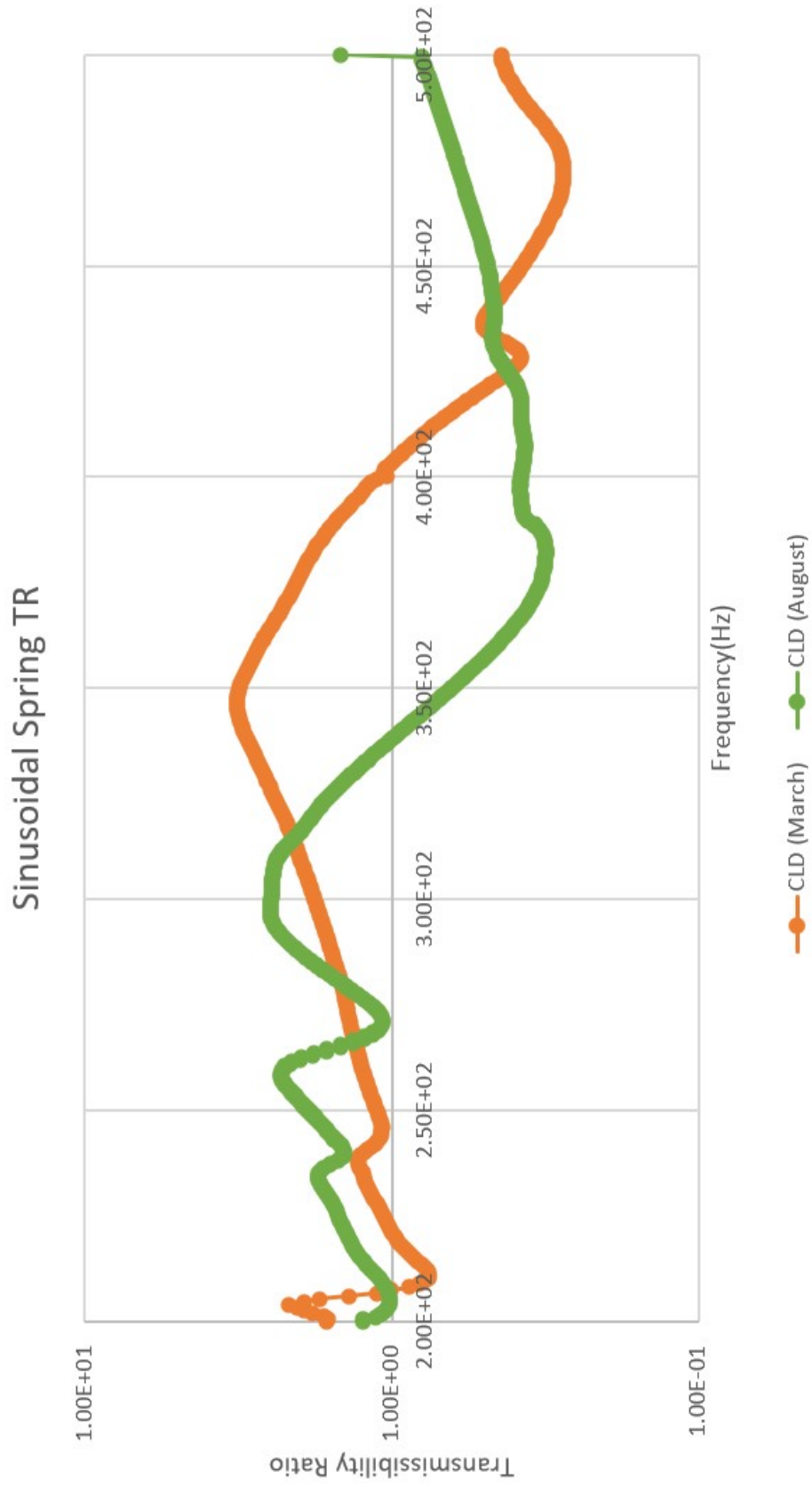


Figure 3.16: CLD Spring Transfer Functions taken 5 Months Apart

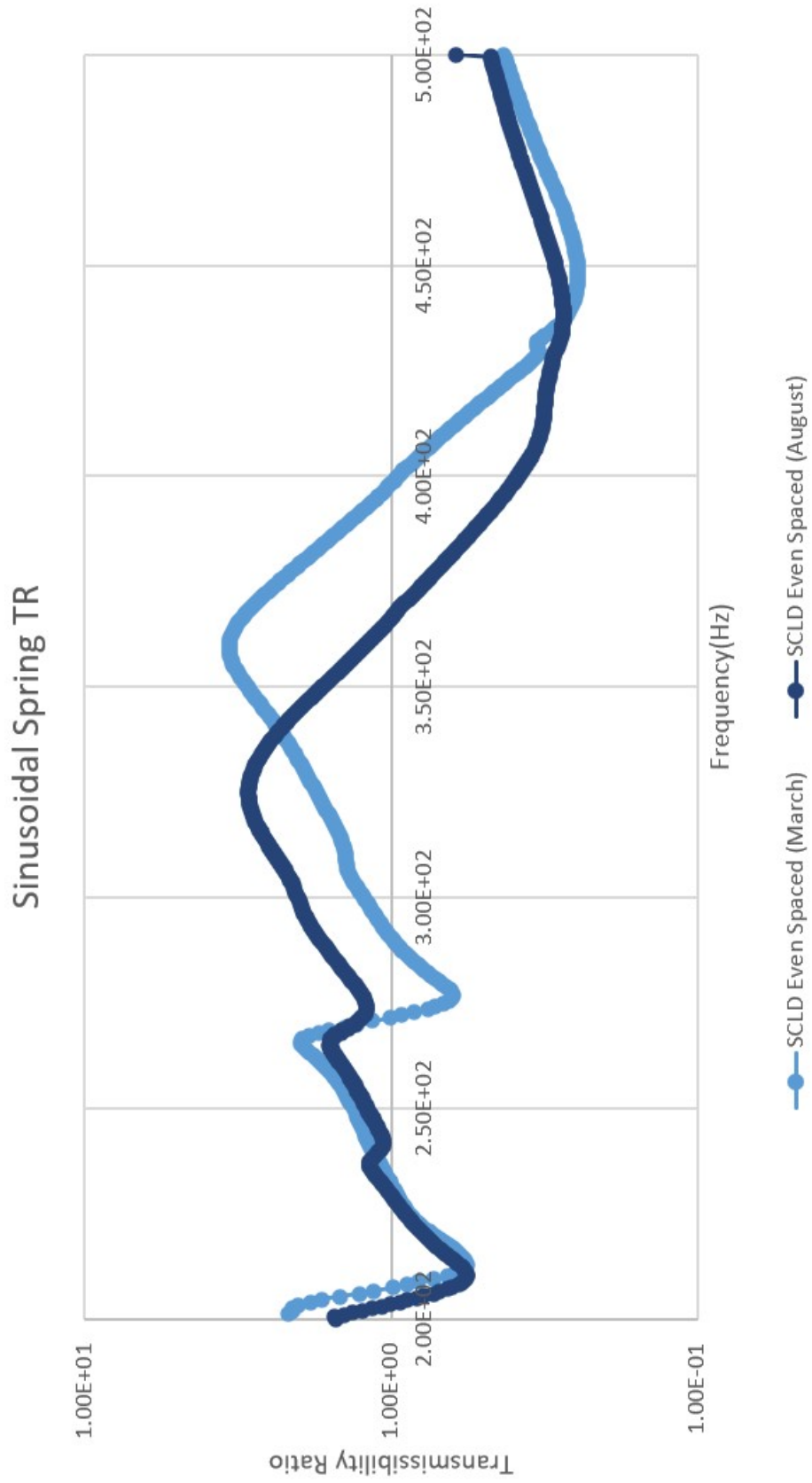


Figure 3.17: SCLD Even Spaced Spring Transfer Functions taken 5 Months Apart

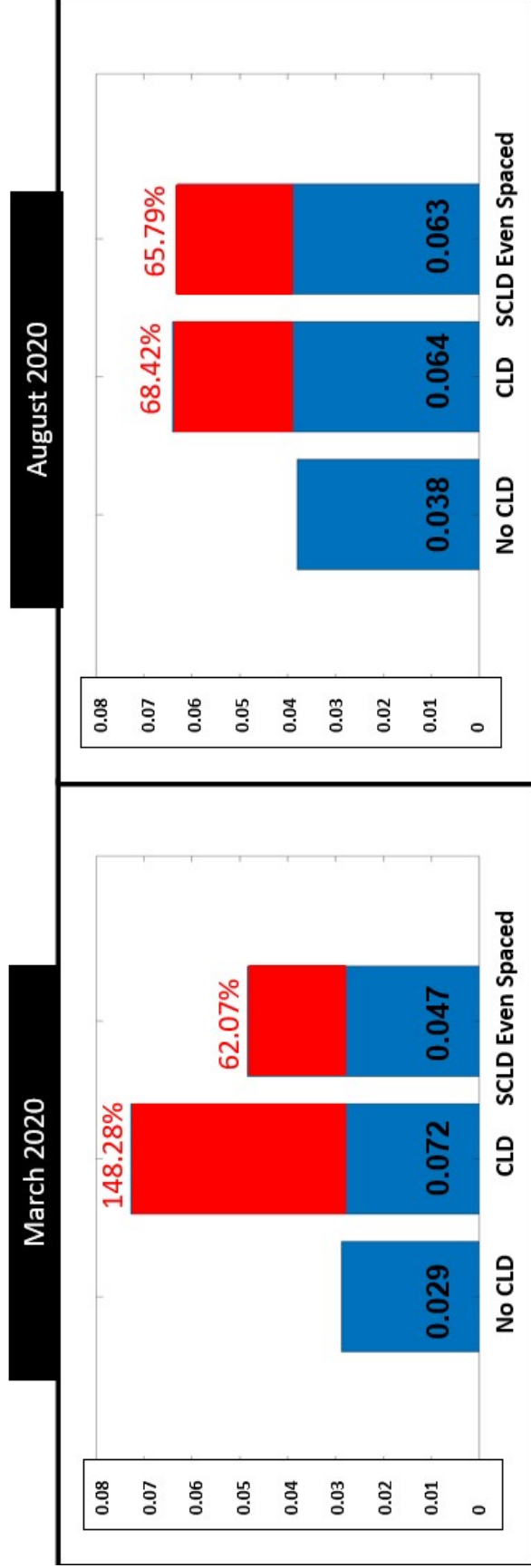


Figure 3.18: Comparison between March and August Damping Ratios (Steady State) for MJM Beams, RED indicates percent increase in damping from the Untreated case.

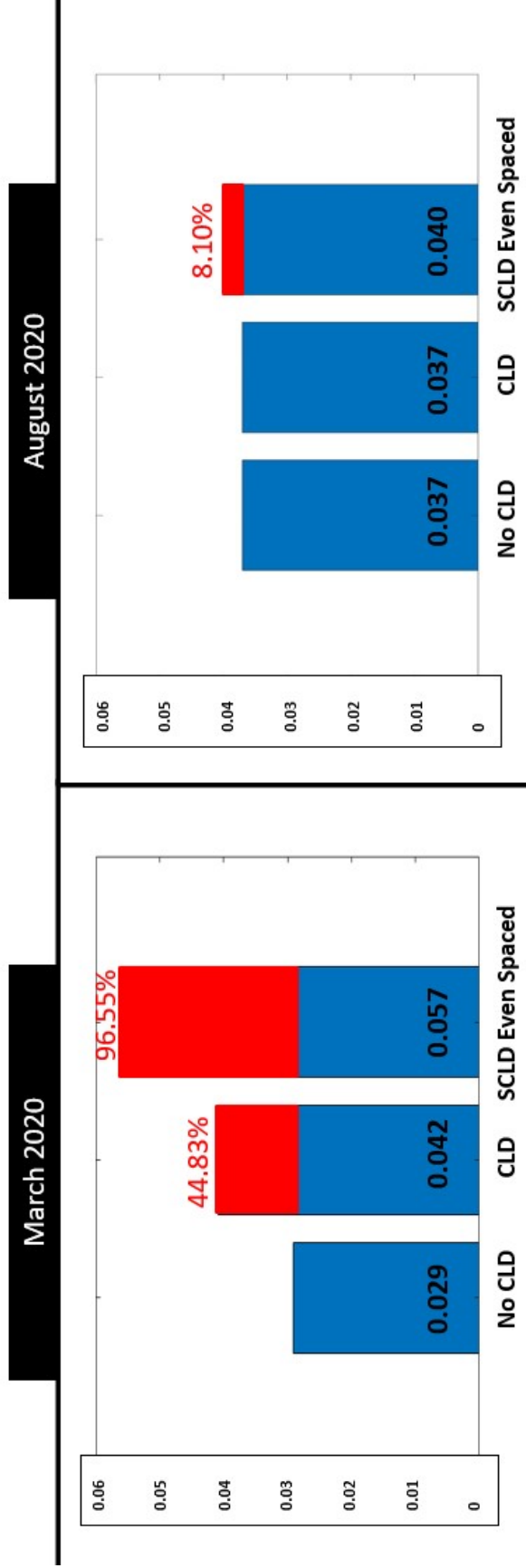


Figure 3.19: Comparison between March and August Damping Ratios (Transient) for MJM Beams, RED indicates percent increase in damping from the Untreated case.

Test Date (2020)	CLD	SCLD Optimized
March	148.28	62.07
August	68.42	65.79

Table 3.3: Percent Increase in Steady State Damping Ratio amongst MJM Springs

Test Date (2020)	CLD	SCLD Optimized
March	44.83	96.55
August	0.00	8.10

Table 3.4: Percent Increase in Transient Damping Ratio amongst MJM Springs

3.5.2 FDM + Hand-layup Spring Results

The FDM Springs were tested for a frequency range of 150-350 Hz. This band contained 3 modes which were used for analysis. Fig. 3.20 shows the delineation between each mode and the local peaks in each zone of the frequency sweep. The image shown reflects transfer functions for the Sinusoidal Springs only, but data was taken for both Rectangular and Sinusoidal configurations overall. Taking data over several modes helped to better emphasize what could classify as a trend in the damping ratio data.

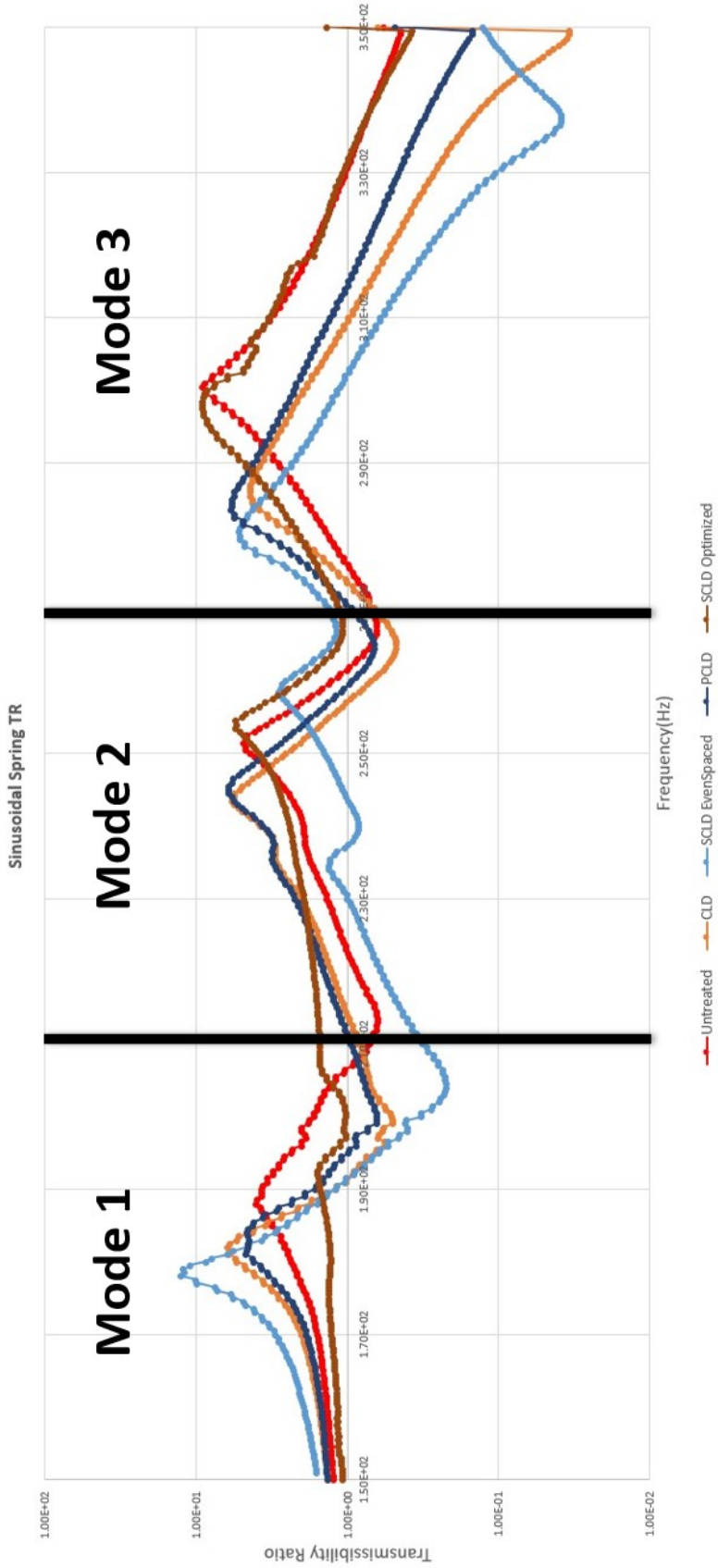


Figure 3.20: Sinusoidal Spring Transmissibility Ratio as a result of Frequency Sweep (150-350 Hz)

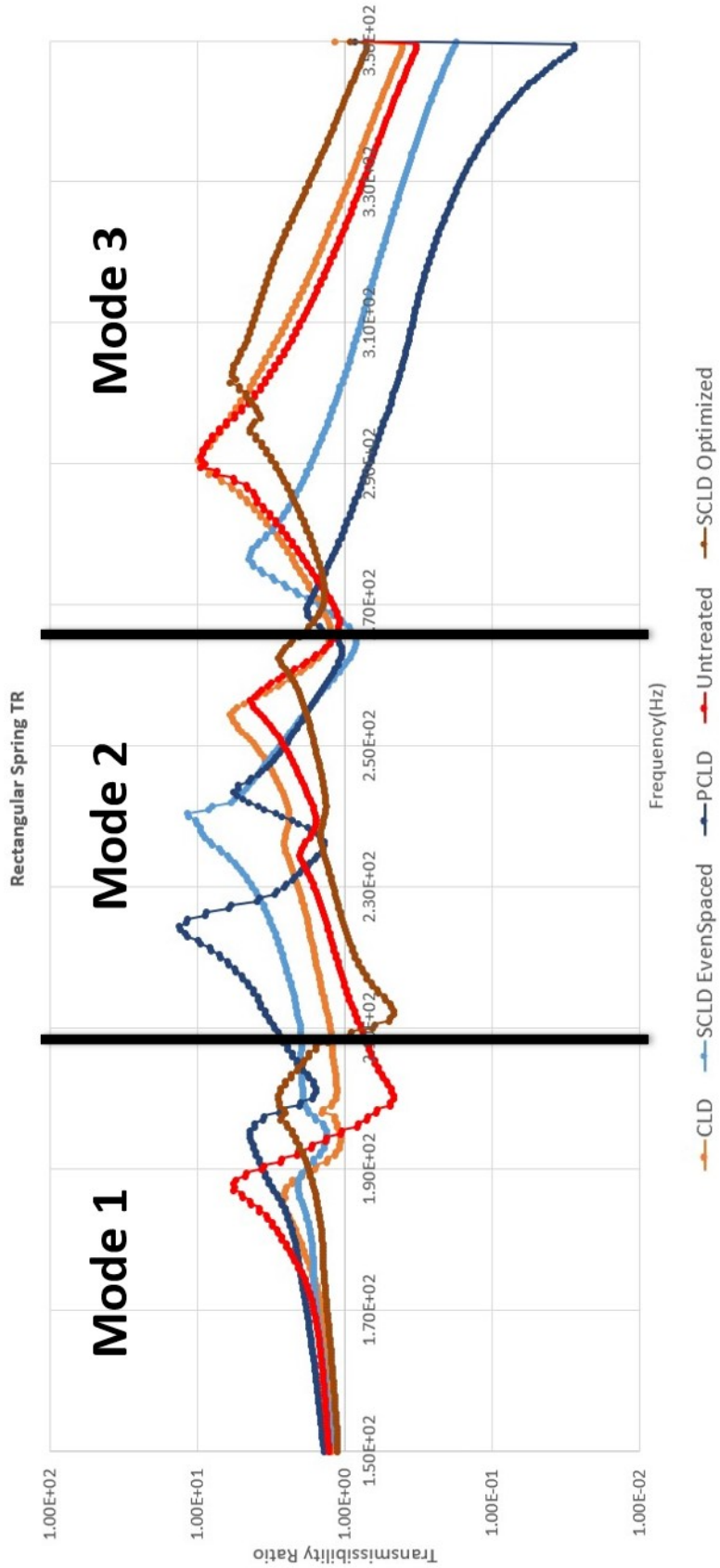


Figure 3.21: Rectangular Spring Transmissibility Ratio as a result of Frequency Sweep (150-350 Hz)

3.5.2.1 Modal Analysis

In this section each mode of the steady state response will be analyzed with respect to damping ratios that coincide with each configuration or category.

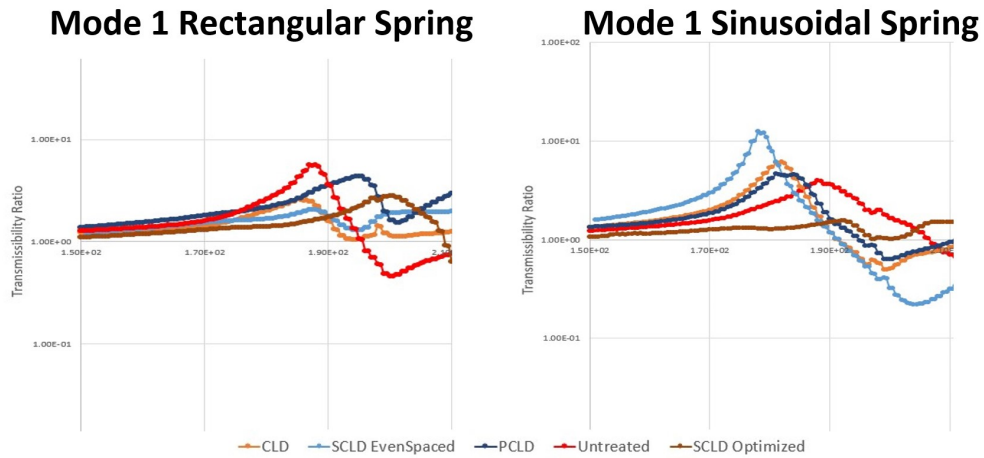


Figure 3.22: Steady State transmissibility functions for Mode 1

Rectangular Springs (FDM)	Steady State Damping Ratio (λ)	Sinusoidal Springs (FDM)	Steady State Damping Ratio (λ)
	Mode 1(187-200 Hz)		Mode 1 (178-192 Hz)
Untreated	0.013	Untreated	0.026
CLD	0.032	CLD	0.019
SCLD Optimized	0.027	SCLD Optimized	0.114
SCLD Even Spaced	0.077	SCLD Even Spaced	0.011
PCLD	0.030	PCLD	0.025

Figure 3.23: Steady State Damping Ratios for Mode 1

Fig. 3.23 brings clarity to the transfer functions shown in Fig. 3.22. The green highlighted cells draw attention to change in damping between the untreated and SCLD optimized (genetic algorithm) cases. For the Rectangular Beam springs, the damping ratio doubles from untreated to SCLD Optimized, but for the SS Spring it increases by a factor of more than 3. The cells highlighted light blue are emphasized

because they show that the Rectangular Beam spring saw increases in damping for each treatment, while this was not the case for the Sinusoidal springs.

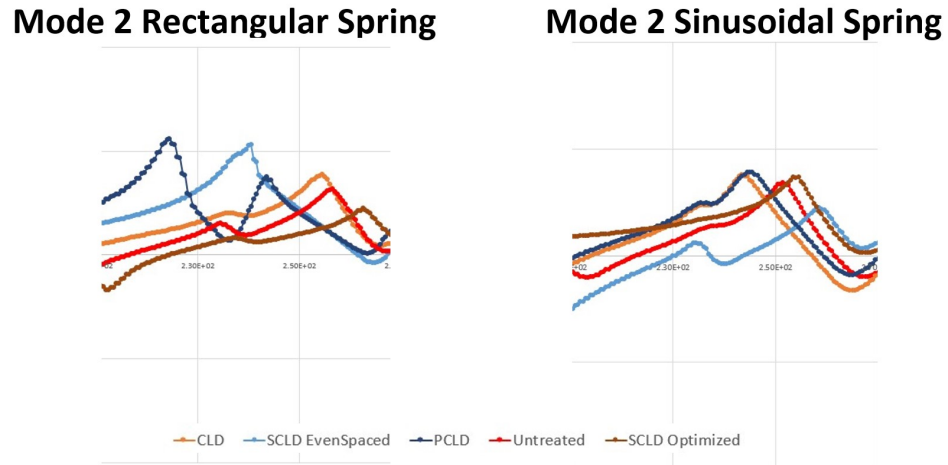


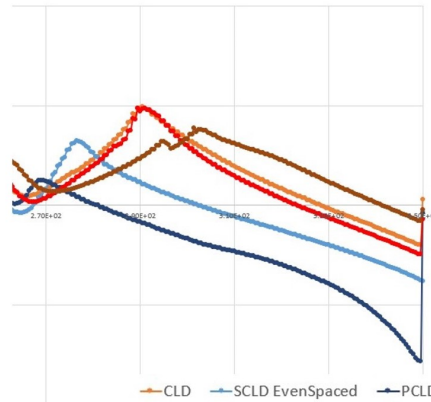
Figure 3.24: Steady State transmissibility functions for Mode 2

Rectangular Springs (FDM)		Sinusoidal Springs (FDM)	
	Mode 2 (225-264 Hz)		Mode 2 (242-257 Hz)
Untreated	0.012	Untreated	0.012
CLD	0.012	CLD	0.014
SCLD Optimized	0.015	SCLD Optimized	0.014
SCLD Even Spaced	0.008	SCLD Even Spaced	0.014
PCLD	0.009	PCLD	0.014

Figure 3.25: Steady State Damping Ratios for Mode 2

Fig. 3.25 brings clarity to the transfer functions shown in Fig. 3.24. Mode 2 did not show significant changes in damping ratio for either spring shape, neither were the changes in damping between treatments noteworthy.

Mode 3 Rectangular Spring



Mode 3 Sinusoidal Spring

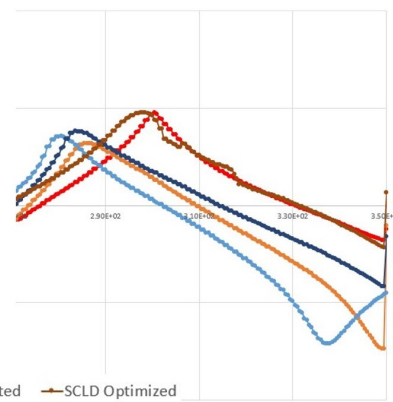


Figure 3.26: Steady State transmissibility functions for Mode 3

Rectangular Springs (FDM)		Sinusoidal Springs (FDM)	
Mode 3 (268-302 Hz)		Mode 3 (280-300 Hz)	
Untreated	0.012	Untreated	0.0115
CLD	0.016	CLD	0.019
SCLD Optimized	0.023	SCLD Optimized	0.017
SCLD Even Spaced	0.011	SCLD Even Spaced	0.014
PCLD	0.020	PCLD	0.0175

Figure 3.27: Steady State Damping Ratios for Mode 3

Fig. 3.27 brings clarity to the transfer functions shown in Fig. 3.26. Once again the cells highlighted light blue are emphasized to show significant increase in damping ratio with respect to the untreated case. Note that for both Rectangular and Sinusoidal Springs, the SCLD Even Spaced treatment was the least effective.

Rectangular Springs (FDM)	Steady State Damping Ratio (λ)		
	Mode 1 (187-200 Hz)	Mode 2 (225-264 Hz)	Mode 3 (268-302 Hz)
Untreated	0.013	0.012	0.012
CLD	0.032	0.012	0.016
SCLD Optimized	0.027	0.015	0.023
SCLD Even Spaced	0.077	0.008	0.011
PCLD	0.030	0.009	0.020

Sinusoidal Springs (FDM)	Steady State Damping Ratio (λ)		
	Mode 1 (178-192 Hz)	Mode 2 (242-257 Hz)	Mode 3 (280-300 Hz)
Untreated	0.026	0.012	0.0115
CLD	0.019	0.014	0.019
SCLD Optimized	0.114	0.014	0.017
SCLD Even Spaced	0.011	0.014	0.014
PCLD	0.025	0.014	0.0175

Figure 3.28: Steady State Damping Ratios: A comparison between Rectangular and Sinusoidal Springs

In Fig. 3.28, the Rectangular Beam spring ratios are compared with those from the Sinusoidal Springs. In this instance, the cells highlighted with green are indicating an increase in damping with respect to the Rectangular Beam version of that same configuration. This is meant to isolate the effect of the structural change on the damping ratio for each damping method. By counting the green cells and the ones that remained the same, one can see that 8/15 damping ratios stayed the same or increased when the sinusoidal structure was implemented.

3.5.2.2 Conclusions

Looking at first resonance of Rectangular and Sinusoidal Springs:

- The damping ratio for the untreated sinusoidal spring was twice that of the rectangular spring (0.026 vs 0.013).

- The GA optimized SCLD treatment had the most impact on the sinusoidal spring (0.026 increased to 0.114)
- The highest damping on the rectangular spring was 0.077, for the evenly spaced SCLD.
- Applying CLD to samples by hand is a major source of inconsistency.

Further discussion and conclusions are contained in Chapter 4.

Chapter 4: Conclusions

Presented in the thesis is an experimental study of segmented constrained layer damping treatments. The different configurations studied include cantilever and axial beam testing, with manufacturing driven by two additive methods in Multi-jet Modeling and Fused Deposition Modeling. A genetic algorithm based configuration for SCLD is also compared with other constrained layer damping methods, in order to isolate the effects of the configuration itself from other factors that are native to all the damping methods used. In addition to testing with cantilever beams in response to a static offset, the optimized configuration and others are applied to sinusoidal spring like structures and the effect of these shapes on passive damping is also analyzed and quantified.

4.1 Beam Experimentation (Phase 1)

Chapter 2 (Phase 1) investigated SCLD damping methods constructed with two kinds of additive manufacturing. When Multi-jet Modeling was used the damping methods (particularly the Optimized method from the genetic algorithm) were effective, being able to increase vibration damping relative to the untreated case both for vibrations of bending beams and for axially vibrating springs. The FDM +

Hand-layup method however, did not yield consistent results for the axial Sinusoidal Springs. The FDM beams included a larger variety of damping configurations and still the CLD and Optimized SCLD beams were shown to increase damping, but the optimized method was severely outperformed. This is suspected to be due to the error that is natural to manual construction process. Beams made with FDM had to have their viscoelastic layers and constraining layers cleaned of loose particles and applied with pressure by hand. The inability to match the dimensional precision all in one process like MJM provides, led to large drop offs in damping ratio. Being able to use and keep the samples over an extended period was an added positive. Both construction methods proved that SCLD is generally more effective when applied with near perfect precision and with the proper materials. Potential sources of error in the FDM beam construction process include:

- Bond strength between essential layers, and intrusive adhesive tape layers
- Foreign particles, air bubbles between layers

The data showed that the GA optimized SCLD strategy which was designed for cantilever beams did work well for the Phase 1 study.

4.2 Sinusoidal Spring Experimentation (Phase 2)

From the Rectangular Beam and Sinusoidal Spring damping ratio results, it is clear that the SCLD Optimized configuration performs better in the first axial vibration mode of both the rectangular and sinusoidal axial spring structures. This

confirms at the very least that the genetic algorithm can provide useful SCLD treatments. No clear trend is seen with the Sinusoidal Springs to support the usefulness of the unique shape. The optimization being intended for beams of specific geometric properties explains why the same trends seen in the Rectangular Springs do not appear with the Sinusoidal Springs.

Though much error is due to the manual and inconsistent application of small layers during construction, past research also suggests that much thinner VE and Constraining Layers must be in play in order to maximize damping [12]. The inconsistency of the data also seems in line with the departure from the guiding assumption [7] of a 4 mm beam base layer used in Chapter 2. Maintaining or increasing the relative thickness of the base structure with respect to the VE and Constraining Layers may improve results.

Overall, the SCLD optimization method is effective when applied without geometrical errors, or weaknesses in the structure. If the MJM materials can be adapted to maintain their original properties, it will make prototyping and testing this kind of treatment much easier. For now, building the treatments by hand is possible but much more care must be taken to the detail of the manufacturing process, as well as to the impact of key variables like cut width, and beam thickness.

4.3 Future Work and Research Implications

Two potential design scenarios were highlighted in Chapter 2. Their purpose was to provide situational, practical value to the results. One was a situation where

the damping treatment is added to an existing surface, and the other was the inclusion of a damping treatment within a constrained cross section or volume. From both perspectives, the FDM method can add significant passive damping capabilities at low cost and without adding much weight. In the case of designing for a constrained volume, weight may even decrease and depending on the application this benefit cannot be overstated. 3D printing offers the unique capability of printing **internal** damping treatments in difficult to reach places. If a printer is made that can print multi-material objects that do not change performance with temperature, it makes such an improvement much easier to implement.

The thesis results need support in the form of predictive models that can take in physical properties and dimensions (number of cuts, layer length, thickness, material properties of each layer) and output a damping ratio. FEA models and numerical models that match the experimentation would increase confidence in the conclusions made.

In addition, the genetic algorithm designed by Al-Ajmi and Bourisli was tested in very limited fashion. In the future tests for beams/springs with:

- varying base thickness
- cut width
- varying viscoelastic material
- alternative to weakening adhesive tape layer
- alternate 3D printed materials

would make conclusions on the algorithm more robust and sturdy.

Research by Guo et al. [30] suggests that there is a connection between the ink-jetting behavior of MJM and viscoelasticity. This suggests that it is a property that can be targeted and optimized, greatly increasing the capacity of the technology to generate fully treated beams specifically for damping vibrations. Also, there is research suggesting the genetic algorithms can also be used to optimize the 3D printed structure itself and not just the cut placement or number of cuts [31]. With the current research confirming that sinusoidal structures can add passive damping through the use of SCLD treatments, topology optimization is a logical step to take. MJM looks to be the future, granted the problems with temperature effects can be solved. In conclusion, the thesis supports not only the genetic algorithm SCLD configuration, but the effectiveness (or lack thereof) of two additive manufacturing methods at producing damped beams, while finally, providing hope that sinusoidal structures can be used creatively to generate more damping from these treatments.

Appendix A: Material Data Sheets

The following appendix contains relevant material properties that were taken from available data sheets and used as reference for design and/or in calculations.

A.1 Material Properties

Materials	Poisson's Ratio
Hard Plastic	0.35
Elastomer	0.49

Table A.1: Assumed Poisson Ratio's

Table [A.1](#) refers to typical values used in industry for the Poisson's ratio of plastic and elastomeric materials. Due to much information on the materials used for research being proprietary, values like Poisson's ratio were taken from materials with similar performance characteristics and scaled minutely when direct values were not provided by manufacturers [\[32\]](#), [\[33\]](#). These Poisson's ratios, along with Young's modulus values from various data sheets, were used to calculate Shear Modulus and to ensure that beam designs aligned with established theory (see Section [2.3](#)). The formula for Shear Modulus used here is:

$$G = E/(2(1 + \mu))$$

with G being Shear Modulus and μ being Poisson's Ratio.

A.1.1 VeroWhite

Poisson's Ratio and other tensile properties are taken from a published source [21].

Materials	Young's Modulus (MPa)	Poisson's Ratio	Shear Modulus (MPa)
VEROWHITE	2500	0.35	925.9

Table A.2: VeroWhite

A.1.2 Agilus30

Poisson's Ratio and other tensile properties are taken from a published source [20].

Materials	Young's Modulus (MPa)	Poisson's Ratio	Shear Modulus (MPa)
Agilus30	1.267	0.49	0.427

Table A.3: Agilus30

A.1.3 ABSplus

Poisson's Ratio and other tensile properties are taken from a published source [23].

Materials	Young's Modulus (MPa)	Poisson's Ratio	Shear Modulus (MPa)
ABSplus	2200	0.35	814.8

Table A.4: ABSplus

A.1.4 Sorbothane

Poisson's Ratio and other tensile properties are taken from a published source [24].

Materials	Young's Modulus (MPa)	Poisson's Ratio	Shear Modulus (MPa)
Sorbothane	0.091	0.49	0.031

Table A.5: Sorbothane

A.1.5 RGD8530

Poisson's Ratio and other tensile properties are taken from a published source [26].

Materials	Young's Modulus (MPa)	Poisson's Ratio	Shear Modulus (MPa)
RGD8530	2400	0.35	925.9

Table A.6: RGD8530

A.1.6 FLX9795

Poisson's Ratio and other tensile properties are taken from a published source [27].

Materials	Young's Modulus (MPa)	Poisson's Ratio	Shear Modulus (MPa)
FLX9795	23.125	0.44	8.030

Table A.7: FLX9795

Appendix B: Analytical Methods for extracting Damping Ratio

B.1 Log Decrement Damping Ratio

The Log Decrement Ratio is a damping estimate that is calculated using consecutive peak amplitudes within a diminishing, oscillating signal. In Fig. [B.1](#) we see these peak points designated as x_1 and x_2 .

$$r = x_1/x_2,$$

$$c = \log(r),$$

$$\lambda = c/\sqrt{(2\pi)^2 c^2}$$

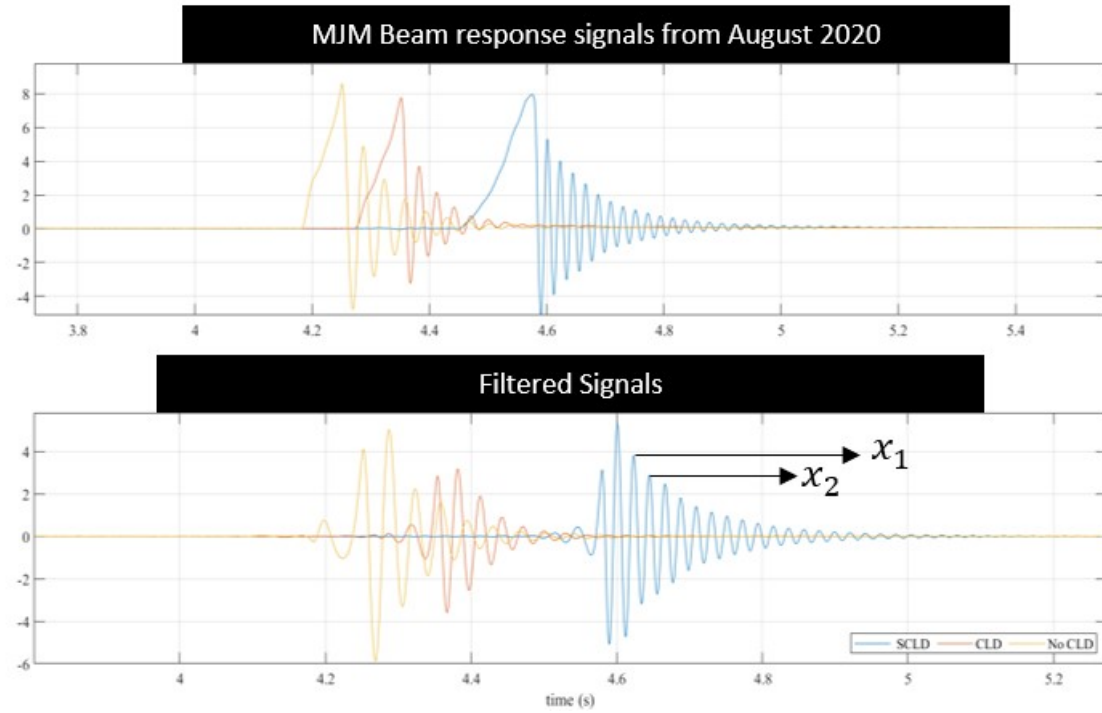


Figure B.1: Raw and Filtered Response Signals from Multi-jet Modeled Beams

Successive Log Decrement Ratios are taken along the envelope, then averaged to produce a single value representing damping for the whole response [34]. Once again, this value λ is what "Damping Ratio" will be referring to during this research. Values of λ showed no evidence of changing significantly with time for the duration of the signals.

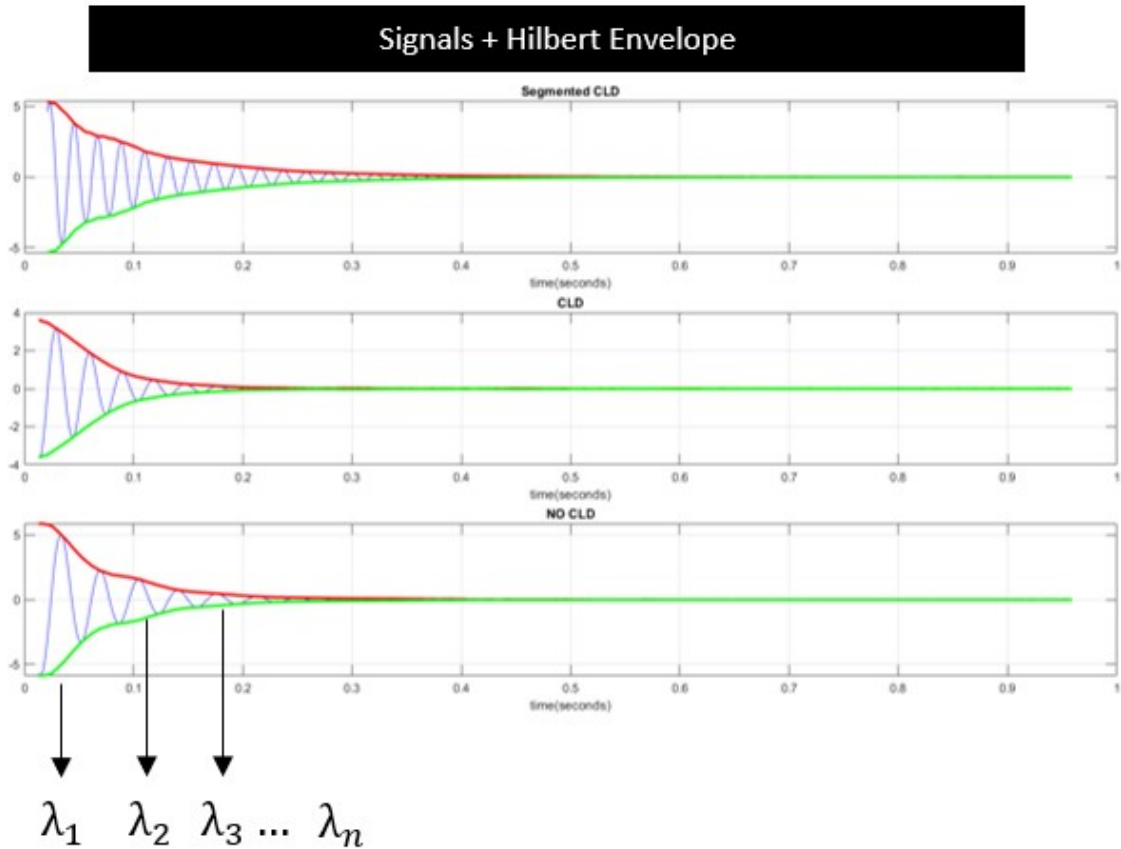


Figure B.2: Filtered Signals after Hilbert Transform is applied

$$\lambda_{signal} = \left(\sum_{k=1}^n \lambda_k \right) / n$$

Fig. B.3 shows that values of λ do not fluctuate much with time. The change with respect to time is taken over a 0.2 second period where the majority of the dampening occurs, and an average of all damping ratios taken along a particular signal is always taken in order to account for the slight inclines that are observed in the trendlines for each set of ratios.

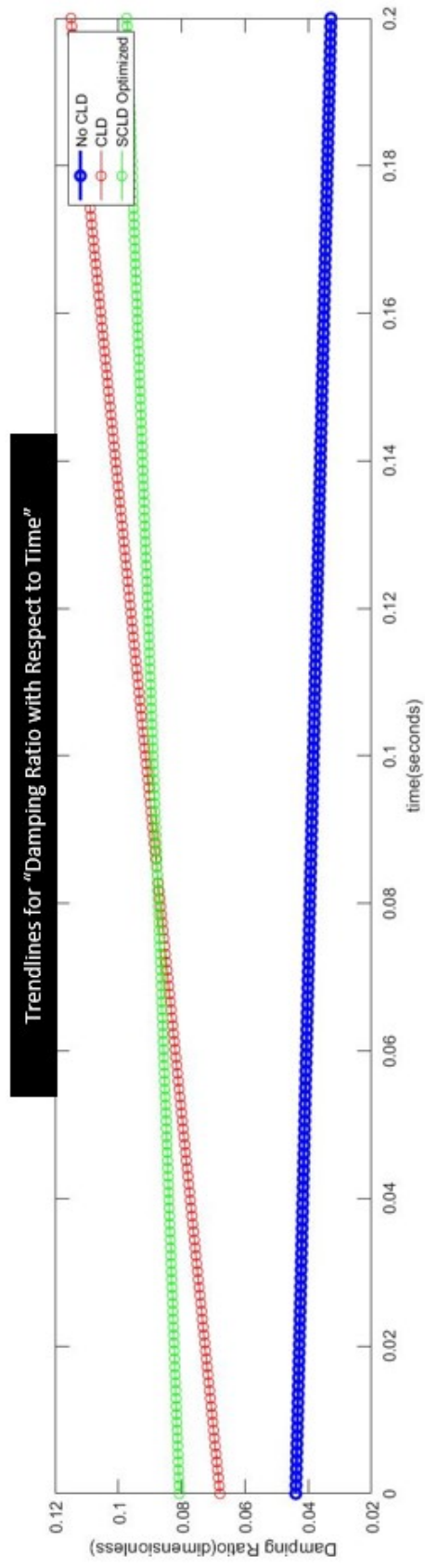
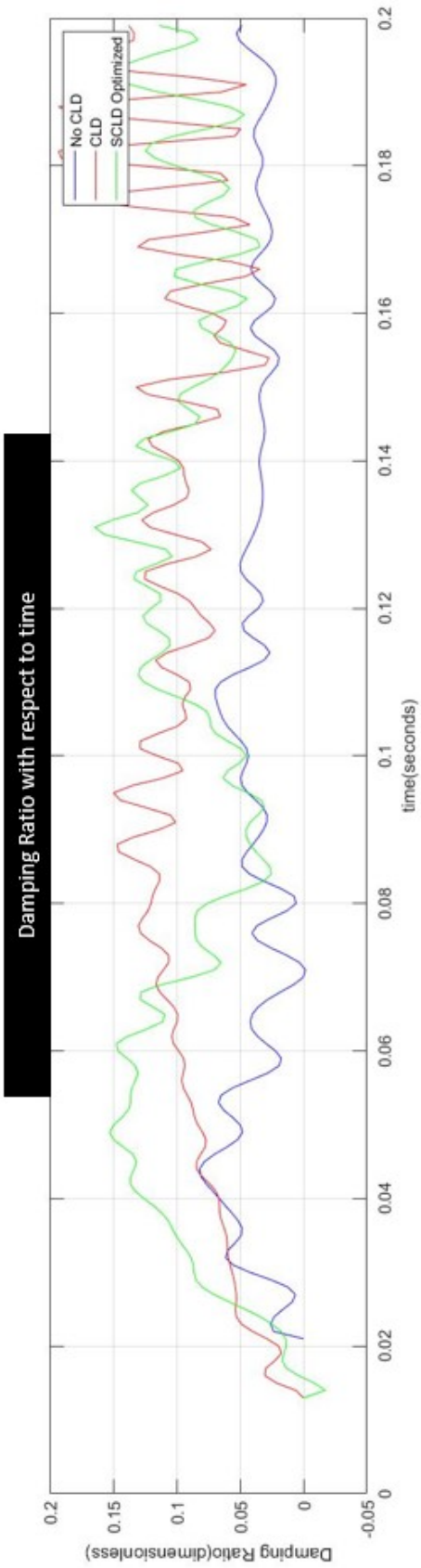


Figure B.3: Change of λ with respect to time

B.2 Half Power Method Damping Ratio

The Half Power Method is used in this chapter to numerically extract damping ratios from transfer functions. It has a high accuracy for damping ratios ≤ 0.05 . The formula is as follows:

$$\lambda = (w_2 - w_1)/(2 * w_n)$$

While w_n is easily found through the location of the resonant peak, frequencies w_2 and w_1 are found through half-power points. The value of the transfer function at resonance (w_n) is synonymous to the system being at full power. The Half Power Method states that w_2 and w_1 can be found by taking the values of your transfer function at half of the full power squared, or:

$$0.5 * (TR_{w_n})^2 = 0.707 * TR_{w_n}$$

The line formed by this value will intersect with the transfer function at w_2 and w_1 , and the difference between these two frequencies can be reliably used to estimate damping ratios that range below 0.05 [34]. Fig. B.4 provides visual aid for how to apply this method to a transfer function. All steady state damping ratios henceforth are generated with this method.

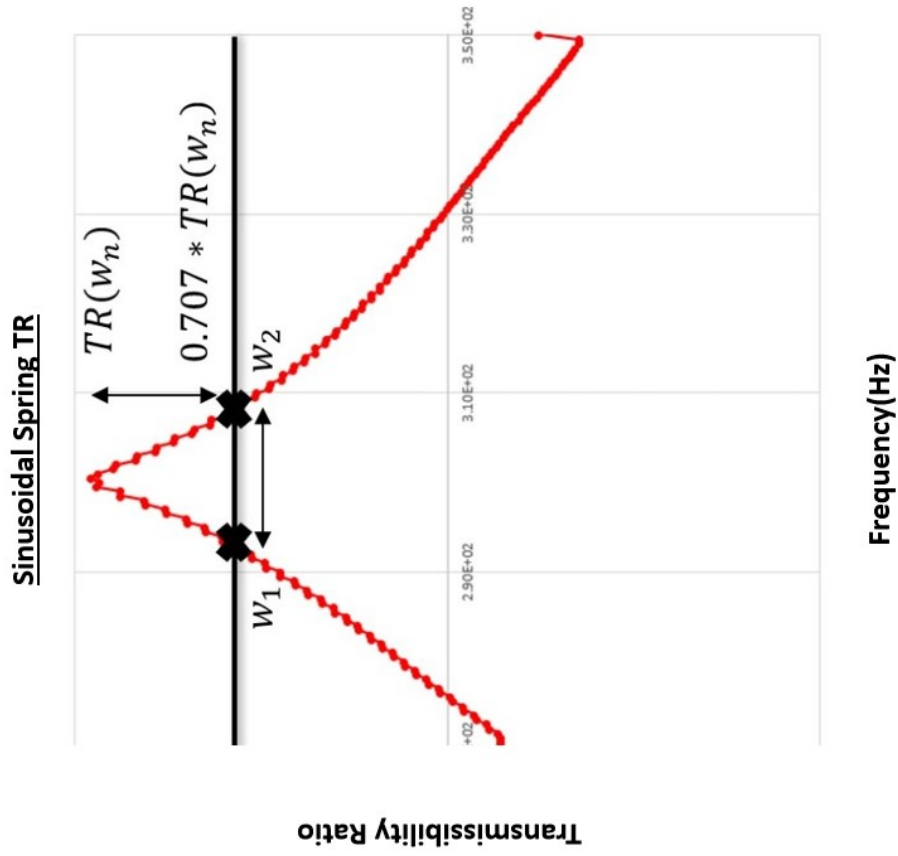


Figure B.4: Half Power Method for Generating Damping Ratio from Transmissibility Ratio

Bibliography

- [1] Mohammed A. Al-Ajmi and Raed I. Bourisli. Optimum design of segmented passive-constrained layer damping treatment through genetic algorithms. *Mechanics of Advanced Materials and Structures*, 15(3-4):250–257, 2008.
- [2] Benjamin Shafer. An overview of constrained-layer damping theory and application. *The Journal of the Acoustical Society of America*, 133(5):3332–3332, 2013.
- [3] George A Lesieutre and Usik Lee. A finite element for beams having segmented active constrained layers with frequency-dependent viscoelastics. *Smart Materials and Structures*, 5(5):615–627, 1996.
- [4] Subhobroto Nath and Norman Wereley. Active constrained layer damping for rotorcraft flex beams. In *36th Structures, Structural Dynamics and Materials Conference(95-1100)*, New Orleans, LA, USA, 1995. AIAA.
- [5] Eric E. Ungar and Edward M. Kerwin. Loss factors of viscoelastic systems in terms of energy concepts. *The Journal of the Acoustical Society of America*, 34(5):741–741, 1962.
- [6] G G Parfitt. The effect of cuts in damping tapes. *Int. Cong. Acoust*, 4th:21–28, Aug 1962.
- [7] Edward M. Kerwin. Damping of flexural waves by a constrained viscoelastic layer. *The Journal of the Acoustical Society of America*, 31(7):952–962, 1959.
- [8] Grégoire Lepoittevin and Gerald Kress. Optimization of segmented constrained layer damping with mathematical programming using strain energy analysis and modal data. *Materials Design*, 31(1):14–24, 2010.
- [9] R. Plunkett and C. T. Lee. Length optimization for constrained viscoelastic layer damping. *The Journal of the Acoustical Society of America*, 48:150, 1969.

- [10] Shitao Tian, Zhenbang Xu, Qingwen Wu, and Chao Qin. Dimensionless analysis of segmented constrained layer damping treatments with modal strain energy method. *Shock and Vibration*, 2016:1–16, 2016.
- [11] Amr M. Baz and Jeng-Jong Ro. In *Smart Structures and Materials 1995: Vibration control of plates with active constrained-layer damping(SPIE -2415)*, San Diego, CA, United States, 1995.
- [12] S C Huang, D J Inman, and E M Austin. Some design considerations for active and passive constrained layer damping treatments. *Smart Materials and Structures*, 5(3):301–313, 1996.
- [13] H V Ganapathy Ram and S Saravanamurugan. Regenerative chatter control in turning process using constrained viscoelastic vibration absorber. *IOP Conference Series: Materials Science and Engineering*, 577:012152, 2019.
- [14] Constrained layer damping. *Noiseless Metal - dB Engineering*.
- [15] C.T. Sun, B.V. Sankar, and V.S. Rao. Damping and vibration control of uni-directional composite laminates using add-on viscoelastic materials. *Journal of Sound and Vibration*, 139(2):277–287, 1990.
- [16] S.-W. Kung and R. Singh. Vibration analysis of beams with multiple constrained layer damping patches. *Journal of Sound and Vibration*, 212(5):781–805, 1998.
- [17] Conor D. Johnson and David A. Kienholz. Finite element prediction of damping in structures with constrained viscoelastic layers. *AIAA Journal*, 20(9):1284–1290, 1982.
- [18] M. Macé. Damping of beam vibrations by means of a thin constrained viscoelastic layer: Evaluation of a new theory. *Journal of Sound and Vibration*, 172(5):577–591, 1994.
- [19] Robert M Haynes. Unpublished notes on carbon fiber coupons and their non-linear force-displacement behavior. 2019.
- [20] StratasyS. Agilus30 digital materials data sheet. Technical report, 2008.
- [21] StratasyS. Verowhite digital materials data sheet. Technical report, 2015.
- [22] StratasyS. “connex3” the versatility standard in 3d printing, white paper. 2017.
- [23] StratasyS. Absplus-430 production grade thermoplastic for 3d printers. Technical report, 2014.
- [24] Sorbothane. Material properties of sorbothane. Technical report, 2018.

- [25] R.f. Kristensen, K.l. Nielsen, and L.p. Mikkelsen. Numerical studies of shear damped composite beams using a constrained damping layer. *Composite Structures*, 83(3):304–311, 2008.
- [26] MatWeb. Rgd8530 digital materials data sheet. Technical report, 2017.
- [27] MatWeb. Flx9795 digital materials data sheet. Technical report, 2017.
- [28] Peter F. Cento and Grzegorz Kawiecki. Evaluation of segmented active constrained layer damping treatments that include bonding layer strain energy. *Smart Structures and Materials 2001: Modeling, Signal Processing, and Control in Smart Structures*, 2001.
- [29] Labworks Inc., 2950 Airway Ave, Costa Mesa, California. *Model ET-139 Electrodynamic Shaker Operation and Installation*.
- [30] Yang Guo, Huseini S. Patanwala, Brice Bognet, and Anson W.k. Ma. Inkjet and inkjet-based 3d printing: connecting fluid properties and printing performance. *Rapid Prototyping Journal*, 23(3):562–576, 2017.
- [31] Andrew T. Gaynor, Nicholas A. Meisel, Christopher B. Williams, and James K. Guest. Multiple-material topology optimization of compliant mechanisms created via polyjet three-dimensional printing. *Journal of Manufacturing Science and Engineering*, 136(6), 2014.
- [32] Performance Plastics. Plastic polymer data sheet. Technical report, 2020.
- [33] Yurijs Shvabs Vladimirs Gonca. Definition of poisson’s ratio of elastomers. *ENGINEERING FOR RURAL DEVELOPMENT*, 2011.
- [34] M J Casiano. Extracting damping ratio from dynamic data and numerical solutions. Technical report, NASA, Huntsville, AL, 2016.